RESEARCH ARTICLE | DECEMBER 30 2025

Numerical simulation of wide-area Kelvin's ship wake based on high-order spectral method

Pengju Bao (包棚举) ; Mingxing Ren (任明星); Fenglai Huang (黄凤来); Decheng Wan (万德成) ; Yuan Zhuang (庄园)

Physics of Fluids 37, 122139 (2025)
https://doi.org/10.1063/5.0308308

Physics of Fluids ARTICLE pubs.aip.org/aip/pof

Numerical simulation of wide-area Kelvin's ship wake based on high-order spectral method

Cite as: Phys. Fluids **37**, 122139 (2025); doi: 10.1063/5.0308308
Submitted: 22 October 2025 · Accepted: 5 December 2025 ·
Published Online: 30 December 2025

Pengju Bao (包棚举),[1] Mingxing Ren (任明星),[2] Fenglai Huang (黄凤来),[3] Decheng Wan (万德成),[1] and Yuan Zhuang (庄园)[1,a)]

AFFILIATIONS

[1]Computational Marine Hydrodynamic Lab (CMHL), School of Ocean and Civil Engineering, Shanghai Jiao Tong University, Shanghai, China
[2]Ningbo Pilot Station, Ningbo Dagang Pilotage Co., Ltd., Ningbo 315020, China
[3]Wuhan Second Ship Design and Research Institute, Wuhan, China

[a)]Author to whom correspondence should be addressed: nana2_0@sjtu.edu.cn

ABSTRACT

The surface wake generated by a vessel sailing on the water surface can persist for kilometers and may disclose navigation parameters. Conventional viscous flow models entail high computational costs for large-scale wake simulation, while potential flow methods also struggle to efficiently capture kilometer-scale wake structures. In this study, the open-source software high-order spectral (HOS)-Ocean, based on the HOS method, is extended to simulate the wide-area wave wakes by inducing a moving surface disturbance. The ship is simplified by a moving two-dimensional (2D) Gaussian pressure distribution. A preliminary analysis is conducted on the effects of pressure distribution steepness, HOS order, and the use of an equivalent inflow condition. Wake structures under varying Froude numbers Fr (based on ship length or water depth) and heading angles θ are analyzed using power spectral density derived from 2D discrete Fourier transform. A preliminary investigation into the effects of environmental waves on wakes is conducted. Results demonstrate distinctive spectral signatures and validate the proposed approach, providing an efficient and reliable framework for wide-area wake prediction in surface vessel operations.

I. INTRODUCTION

Advanced surface vessels play a crucial role in ensuring maritime security. When a vessel navigates at a certain speed, it inevitably generates a wake that is confined within a triangular wedge-shaped region and persists over a wide area of the sea. By simplifying a ship into a "point pressure" source moving on the free surface, Kelvin first proposed and theoretically predicted the range of wave systems, namely, the famous Kelvin angle, $\theta_{\text{Kelvin}} = \sin^{-1}(1/3) \approx 19.47°$, a value that remains constant irrespective of the vessel's velocity.[1] Furthermore, the wake is comprised of both transverse waves and divergent waves.

However, it should be noted that in practice, wake characteristics are subject to variation due to factors such as ship velocity and the configuration of the hull. Rabaud and Moisy[2] analyzed airborne images of ship wakes and discovered that at high speeds, the wake angle appears to be inversely proportional to the ship's velocity. Subsequently, Darmon *et al.*[3] further investigated the wake using a moving axisymmetric pressure field model. They concluded that at high Froude numbers based on hull length, the angle of maximum wave amplitude scales inversely with the Froude number, while the overall wake remains confined within the classical Kelvin wedge. Miao and Liu[4] conducted a study on arbitrary pressure distributions. They found that the apparent wake angle[5] was defined by the highest wave peaks, and most pressure distributions were scaled as the inverse first power of the Froude number. However, for specific non-smooth pressure disturbances, they followed with inverse square relationship. Pethiyagoda *et al.*[6] considered the limit at low Froude numbers, where transverse waves dominate, and found that the apparent wake angle decreases as the Froude number is reduced. Additionally, Moisy and Rabaud[7] extended their analysis to non-axisymmetric pressure fields resembling those of real ships, investigating how the aspect ratio of the pressure distribution influences the maximum amplitude of waves in the far field.

The characteristics of the wake left behind the moving object can reveal information about the structural and navigational parameters of the vessel. The wake pattern provides direct evidence of the vessel's heading, while the lateral displacement between the vessel and its wake allows for an estimation of its speed.[8] Graziano *et al.*[9] determined the ship's heading from the orientation of its turbulent wake and estimated

the velocity based on the azimuthal drift and the wavelength of the Kelvin wake pattern. Recent studies have increasingly adopted spectrogram-based approaches for the systematic examination of ship wake signatures. This emerging methodology enables detailed time-frequency characterization of wake components, particularly facilitating the identification and analysis of transverse and divergent wave systems within the complex wake structure.[10–13] Spectral analysis of the wake field also enables the decomposition of its constituent components, thereby supporting the estimation of vessel heading, speed, and hull geometry.[14–16] Furthermore, Kelvin wake systems may impose impacts on coastal and riverine banks, harbor infrastructures, as well as vessels moored along shorelines. The persistent wave energy and resulting hydrodynamic forces can potentially affect structural integrity and operational safety in these marine environments.[17–21] Therefore, research into wide-area wakes is of great significance.

In these studies,[2–4,6,7] the hull is approximated as a pressure distribution moving on a free surface, with the most widely used being the Gaussian pressure distribution with single peak. The distinction lies in whether the distribution is axisymmetric. Non-axisymmetric distributions are closer to actual ship hulls than axisymmetric distributions. Nevertheless, due to the smooth mathematical properties of the unimodal Gaussian pressure distribution, it cannot adequately characterize the abrupt changes in shape at the bow, stern, and ship board.[22] Consequently, the wake calculated utilizing this distribution will necessarily exhibit discrepancies compared to the actual wake. Lo[23] examined two extreme cases of hull-shape functions: a sharp rectangular shape and a smooth Gaussian shape. Comparison with both experimental and simulated data demonstrates that a realistic hull is expected to yield results intermediate to these two extremes. Employing a similar Gaussian-distributed pressure source term, Paprota[24] combined the Fourier–Galerkin method to implement rapid wake prediction within the MATLAB environment and explored wave patterns for multiple pressure distributions.

The wake generated by a real vessel in open ocean can extend over kilometers, necessitating numerical computational domains of comparable scale. Conventional numerical methods face significant challenges in simulating Kelvin wake systems in open seas. These approaches require extensive computational domains and carefully designed boundary conditions to maintain sufficient distance between the body and domain boundaries, thereby avoiding nonphysical reflections. However, this requirement prevents efficient simulation of complete wave systems. For instance, when using traditional viscous flow theory to solve the Navier–Stokes equations for ship-generated waves, the complete wave system during ship–wave interaction cannot be fully captured due to domain constraints in computational fluid dynamics (CFD) simulations. The presence of lateral constrictions in navigational channels creates a fundamentally different wave regime from open-water conditions. As ship-induced waves impinge upon the confining banks, they experience successive reflections that generate secondary wave systems. These persistent wave interactions produce a complicated superposition pattern that evolves continuously along the waterway.[25–28] Furthermore, wave absorption zones must be implemented to prevent wave reflection, which expands the required computational domain and reduces efficiency. The computational cost and time requirements become substantial under these conditions, while numerical dissipation arising from insufficient grid resolution in large domains further degrades solution accuracy, rendering its practical implementation particularly challenging.

While potential flow theory offers improved computational efficiency for wave problems, simulating the full wake field still requires substantial resources. The method proposed by Paprota[24] achieves higher computational speed; however, its use of a modified Euler iterative scheme introduces some trade-offs in accuracy. In contrast, the high-order spectral (HOS) method, originally developed by Dommermuth and Yue,[29] employs a pseudo-spectral approach combined with fast Fourier transforms (FFT), yielding exceptionally rapid convergence. Ducrozet *et al.*[30] subsequently created the open-source software HOS-Ocean based on this method, which efficiently simulates nonlinear wave propagation over extensive oceanic areas. Nevertheless, despite relaxed requirements for computational grids and time steps, the presence of the object was not taken into account, resulting in the failure to generate the surface wake.

Consequently, the development of a numerical approach that can effectively simulate open-sea conditions while minimizing boundary reflection effects, and simultaneously achieve efficient generation and evolution of complete Kelvin wake systems, could help address current computational challenges while providing useful references for wake pattern analysis, potentially supporting further investigations in this field. Accordingly, this research builds upon the HOS method and augments the open-source model HOS-Ocean by incorporating a surface-moving Gaussian pressure distribution to represent the ship's effect, thereby achieving efficient simulation of ship-generated wakes in open seas and providing a reliable foundation for further studies on large-scale ship-generated wave patterns. In addition to the pressure distribution approximation, alternative approaches such as the boundary element method (BEM) can be employed to represent the presence of structures for wave modeling[31–37] and so on,[38,39] although these methodologies are not addressed in the present study. Additionally, it should be acknowledged that this study is conducted within the potential flow framework, which excludes viscous effects and neglects the air–water boundary layer (despite its thinness).[40,41] Viscous ship waves exhibit a larger apparent wake angle compared to pure gravity waves, with viscous effects inducing energy dissipation that leads to amplitude attenuation over propagation distance—divergent waves being particularly susceptible.[42–47] Inviscid models tend to overestimate far-field wave heights due to the absence of such dissipation. Asymptotic analysis and perturbation methods can provide quantitative descriptions of this attenuation behavior.[48–55] Furthermore, when viscosity is considered, wave-breaking phenomena may also occur under certain conditions.[56–58] Future refinements could incorporate corresponding correction terms to address these physical phenomena, though such considerations remain beyond the scope of the current investigation.

Notably, although the Gaussian pressure distributions employed across these studies[7,23,24] share a broadly consistent functional form, the specific coefficient within the exponential term often varies. The impact of this parameter choice on the resulting wake features remains inadequately quantified, and there appears to be neither a clear

consensus nor a rigorously justified value for its selection. Therefore, an exploratory analysis of the influence of this coefficient's value on the wake structure will also be conducted.

In Sec. II, the details of HOS, pressure distribution term, and the workflow in modified HOS with wakes are introduced. In Sec. III, the method validation and related discussions (shape factor β, HOS order M, and usage of current) are detailed, and the wake corresponding to different Froude numbers Fr (based on ship length or water depth) and heading angles θ is calculated, and a preliminary investigation into the effects of environmental waves on wakes has been conducted. The conclusions and outlooks are drawn in Sec. IV.

II. NUMERICAL METHOD

A. High-order spectral method

High-order spectral (HOS) method is grounded in potential flow theory, which rests on the fundamental assumptions that the fluid is incompressible, and the flow is inviscid and irrotational. Following the method proposed by Zakharov,[59] the surface velocity potential ϕ^s is introduced:

$$\phi^s(\boldsymbol{x},t) = \phi(\boldsymbol{x},\eta,t), \tag{1}$$

where $\boldsymbol{x} = (\boldsymbol{x},\boldsymbol{y})$ denotes the horizontal coordinates; ϕ and η represent the velocity potential and free-surface elevation, respectively; and t indicates time. Assume that ϕ and η are $O(\epsilon)$ and that the wave steepness $\epsilon = kA$ must be much less than 1, where k is the wavenumber and A is the wave amplitude. The velocity potential ϕ can be expanded asymptotically as a perturbation series and expanded as a Taylor series about $z = 0$ (the still water level) and truncated at the same order M, yielding

$$\phi^s(\boldsymbol{x},t) = \phi(\mathbf{x},\eta,t) = \sum_{m=1}^{M}\sum_{k=0}^{M-m}\frac{\eta^k}{k!}\frac{\partial^k}{\partial z^k}\phi^{(m)}(\boldsymbol{x},0,t). \tag{2}$$

Substituting these into the free-surface boundary conditions yields the equations for ϕ^s and η,

$$\eta_t + \nabla_x\phi^s\cdot\nabla_x\eta - (1+\nabla_x\eta\cdot\nabla_x\eta) \times\left[\sum_{m=1}^{M}\sum_{k=0}^{M-m}\frac{\eta^k}{k!}\sum_{n=1}^{N}\phi_n^{(m)}(t)\frac{\partial^{k+1}}{\partial z^{k+1}}\psi_n(\boldsymbol{x},0)\right] = 0, \tag{3}$$

$$\phi_t^s + g\eta + \frac{1}{2}\nabla_x\phi^s\cdot\nabla_x\phi^s - \frac{1}{2}(1+\nabla_x\eta\cdot\nabla_x\eta) \times\left[\sum_{m=1}^{M}\sum_{k=0}^{M-m}\frac{\eta^k}{k!}\sum_{n=1}^{N}\phi_n^{(m)}(t)\frac{\partial^{k+1}}{\partial z^{k+1}}\psi_n(\boldsymbol{x},0)\right]^2 \times + \frac{P}{\rho} = 0, \tag{4}$$

where the subscript t denotes partial derivative with respect to time, and the differential operator ∇_x represents spatial derivatives. The term $\phi_n^{(m)}$ denotes the m th order velocity potential at the n th mode, while ψ_n represents the corresponding eigenfunction.[29] The symbol g denotes gravitational acceleration, η the free-surface elevation, and ρ the fluid density. The term P represents pressure. In the absence of free-surface disturbances, it is defined as relative pressure and taken to be zero; otherwise, it corresponds to a surface pressure distribution term representing perturbations on the free surface.[60] A detailed description of the pressure distribution term introduced in this study will be provided in Sec. III B.

B. Pressure distribution term

When a ship advances at a constant speed on the free surface, its disturbance generates a wake. To simulate the capture of this wake using HOS-Ocean, a moving pressure distribution term P must be introduced into the dynamic free-surface boundary condition [Eq. (4)] to represent the disturbance induced by vessel motion. It should be noted that only a stationary pressure distribution moving uniformly over the free surface is considered in this approach; temporal and spatial variations in pressure around the hull during actual navigation, as well as the ship's own oscillatory motions, are neglected. Let $\boldsymbol{x} = (x,y)$ and $\boldsymbol{u} = (U,V)$ denote the horizontal coordinates and velocity vector, respectively, and the general form is given by the following equation:

$$P = P(\boldsymbol{x},t) = P(\boldsymbol{x}-\boldsymbol{u}t). \tag{5}$$

The hull is simplified as a pressure distribution characterized by the product of a peak coefficient $p_0 = \rho g D$ and a shape factor $S(x,y)$, where D can be assigned a draft value. Mathematically, the formulation may be viewed as the transformation of a uniformly pressurized rectangular region into a target pressure distribution through a specifically designed shape factor $S(x,y)$. This method preserves advantageous geometric characteristics while providing a reasonable approximation of hull-induced surface disturbances. From a physical standpoint, building upon the hydrostatic relation $P = \rho g\eta$, the static pressure distribution of the hull is employed to approximate the dynamic disturbances generated during ship motion. Within this framework, $D\cdot S(x,y)$ describes the local draft function across the hull surface, where D may be selected as either the mean or maximum draft. While the specific determination of this parameter warrants case-specific adjustment and its influence requires systematic comparative analysis. The draft value applied in this study specifically corresponds to that employed in the referenced literature[23] for the same vessel configuration, maintaining consistency for comparative purposes, while the influence of this parameter has not been systematically analyzed in the current investigation. The choice of the shape factor is arbitrary; examples include those used for Wigley hulls or in the pressure distributions employed by Doctors and Sharma.[63] A normalized Gaussian function is adopted as the shape factor in this study

$$S(x,y) = e^{-\frac{1}{2(1-r^2)}\left[\left(\frac{x-\mu_x}{\sigma_x}\right)^2 - 2r\frac{x-\mu_x}{\sigma_x}\frac{y-\mu_y}{\sigma_y} + \left(\frac{y-\mu_y}{\sigma_y}\right)^2\right]}, \tag{6}$$

where μ_x and μ_y represent the coordinates of the peak center of the shape factor, while σ_x and σ_y denote its spatial extents in the longitudinal and transverse directions, respectively. The parameter r further characterizes the shape properties of the distribution, and usually, $r = 0$ is taken. Then, the shape factor can be

$$S(x,y) = e^{-\frac{1}{2}\left[\frac{(x-\mu_x)^2}{\sigma_x^2} + \frac{(y-\mu_y)^2}{\sigma_y^2}\right]}. \tag{7}$$

Figure 1 illustrates the distribution corresponding to Eq. (7), with its center located at the origin (i.e., $\mu_x = 0$, $\mu_y = 0$). By assigning different values to σ_x and σ_y, the resulting shape, as observed in the top view, exhibits an elliptical profile. Currently, the long axis of the shape factor is parallel to the x axis. Rotate it counterclockwise by an angle θ, and the coordinates after rotation are

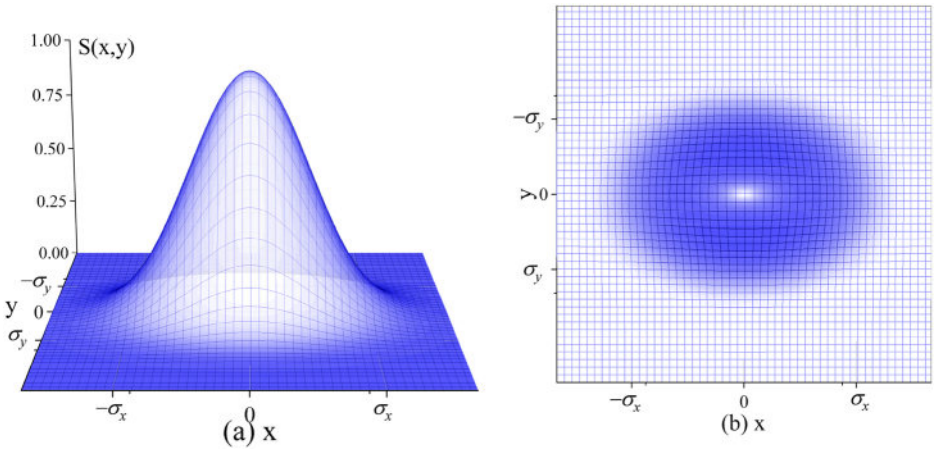

FIG. 1. The shape factor $S(x, y)$ described in Eq. (7). (a) Three-dimensional view and (b) top view.

$$\begin{cases} x' = x\cos\theta + y\sin\theta, \\ y' = -x\sin\theta + y\cos\theta, \end{cases} \tag{8}$$

where x' and y' denote the coordinates after rotation, serving as intermediate variables in the mathematical formulation. For consistency, the original coordinates x and y will be retained in subsequent discussions. Subsequently, $S(x, y)$ is expressed as follows:

$$S(x,y) = e^{\left[-\left(\gamma_x(x-\mu_x)^2+2\gamma_{xy}(x-\mu_x)(y-\mu_y)+\gamma_y(y-\mu_y)^2\right)\right]}, \tag{9}$$

where symbol γ is defined as

$$\gamma_x = \frac{\cos^2\theta}{2\sigma_x^2} + \frac{\sin^2\theta}{2\sigma_y^2}, \tag{10}$$

$$\gamma_{xy} = \frac{\sin 2\theta}{4\sigma_x^2} - \frac{\sin 2\theta}{4\sigma_y^2}, \tag{11}$$

$$\gamma_y = \frac{\sin^2\theta}{2\sigma_x^2} + \frac{\cos^2\theta}{2\sigma_y^2}. \tag{12}$$

Consider the ship length L_s, beam B_s, draft D_s, and rotation angle θ_s, if the shape dimensions at S_{peak}/a ($a > 1$ is a constant denoting peak ratio) in Eq. (9) are used to characterize the ship geometry, then

$$\sigma_x = \frac{L_s}{2\sqrt{2\log(a)}}, \quad \sigma_y = \frac{B_s}{2\sqrt{2\log(a)}}. \tag{13}$$

In the present study, the pressure distribution is assumed to move uniformly in the positive x direction at a constant horizontal velocity U, while $V = 0$. Denoting time as t, the general form of the pressure distribution term can accordingly be expressed as

$$P = P(x, y, t) = P(x - Ut, y). \tag{14}$$

For such a case, the ship's angle of rotation is zero, i.e., $\theta_s = 0$, and by submitting this into Eq. (13), one can obtain: $\gamma_x = \frac{4\log(a)}{L_s^2}$, $\gamma_{xy} = 0$, and $\gamma_y = \frac{4\log(a)}{B_s^2}$, then the shape factor and the pressure distribution can be written as Eqs. (15) and (16), respectively,

$$S(x,y) = e^{-4\log(a)\left[\frac{(x-\mu_x)^2}{L_s^2}+\frac{(y-\mu_y)^2}{B_s^2}\right]}, \tag{15}$$

$$\begin{aligned} P(x-Ut,y) &= \rho g D_s \cdot S(x-Ut,y) \\ &= \rho g D_s \cdot e^{-4\log(a)\left[\frac{(x-\mu_x-Ut)^2}{L_s^2}+\frac{(y-\mu_y)^2}{B_s^2}\right]}. \end{aligned} \tag{16}$$

The two-dimensional (2D) Fourier transform converts a function from the spatial domain (x, y) to the frequency domain (u, v). For a Gaussian function, its Fourier transform remains a Gaussian function. For a standard Gaussian shape such as that in Eq. (7), its Fourier transform is given by the following equation:

$$\hat{S}(u,v) = 2\pi\sigma_x\sigma_y e^{-2\pi^2\left(\sigma_x^2u^2+\sigma_y^2v^2\right)} e^{-i\cdot 2\pi(\mu_x u+\mu_y v)}. \tag{17}$$

The Fourier transform of Eq. (9) is given by the following equation:

$$\hat{S}(u,v) = \frac{\pi}{\sqrt{\gamma_x\gamma_y-\gamma_{xy}^2}} e^{-\frac{\pi^2}{\gamma_x\gamma_y-\gamma_{xy}^2}\left(\gamma_y u^2-2\gamma_{xy}uv+\gamma_x v^2\right)} e^{-i\cdot 2\pi(\mu_x u+\mu_y v)}. \tag{18}$$

Accordingly, the pressure distribution [Eq. (16)] can be depicted in the frequency domain as follows:

$$\begin{aligned} \mathcal{F}[P(x-Ut,y)] = \rho g D_s \cdot \frac{\pi L_s B_s}{4\log(a)} \\ \cdot e^{-\frac{\pi^2}{4\log(a)}\left(L_s^2u^2+B_s^2v^2\right)} e^{-i\cdot 2\pi\left((\mu_x+Ut)u+\mu_y v\right)}. \end{aligned} \tag{19}$$

The introduction of a translation term $x - Ut$ in the spatial domain, according to the shift property of the Fourier transform, implies the introduction of a phase factor $e^{-i\cdot 2\pi(Ut\cdot u)}$ in the frequency domain.

C. Wake solver workflow

The large-domain wake solver is generated based on HOS-Ocean. HOS-Ocean is an open-source solver released in 2016 by the LHEEA Laboratory at École Centrale de Nantes. It is based on the high-order spectral (HOS) method and is specifically designed for simulating the propagation of nonlinear wave fields over constant finite depth in open ocean. Due to its use of periodic boundary conditions, the solver does not include a separate wave generation boundary. Instead, the simulation is initialized by specifying the initial surface elevation and velocity potential of the wave field.

Prior to computation, the solver processes user-defined parameters from an input file to configure the numerical scheme and physical conditions. Most of these parameters are dimensionless using characteristic wavelength and wave period as scaling factors. During initialization, relevant physical quantities—such as computational domain size and simulation duration—are similarly dimensionless. This scaling strategy serves two key purposes: it reduces round-off errors caused by large disparities in numerical magnitudes and relaxes the constraints on spatial and temporal discretization when simulating large domains. As a result, both computational efficiency and numerical stability are significantly enhanced.

As illustrated in Fig. 2, a rectangular computational domain is considered, with its coordinate origin located at the bottom-left corner. The positive z axis is oriented outward, normal to the plane. The dimensionless parameters *xlen* and *ylen* represent the number of wavelengths in the x and y directions, respectively. Taking deep-water conditions as an example, Fig. 3 demonstrates the dimensionless procedure: based on the input significant wave period Tp_{real}, the significant wavenumber kp_{real} and wavelength λ_h are derived. These are used to define the characteristic length scale L and timescale T, which in turn facilitate the normalization of the total simulation duration T_{stop}, as well as the domain dimensions $xlen_{tot}$ and $ylen_{tot}$. This process yields the corresponding dimensionless parameters *time*, $xlen_{star}$, and $ylen_{star}$. In the output phase, a scaling parameter is used to determine whether results should be presented in dimensional or non-dimensional form, allowing convenient comparison across computational domains of different physical scales.

After being introduced into HOS-Ocean and rendered dimensionless, the final expression for the pressure distribution term is obtained as follows:

$$\frac{P(x-Ut,y)}{\rho} = \alpha \cdot e^{-\beta \cdot \left[\frac{(x-X)^2}{L_s^2}+\frac{(y-Y)^2}{B_s^2}\right]}, \tag{20}$$

where $\alpha = g_{star} \cdot \frac{D_s}{L}$ is the dimensionless peak value and $g_{star} = \frac{g}{L/T^2}$ is the dimensionless gravity acceleration, $\beta = 4\log(a)$ represents the shape parameter, and $X = \mu_x + Ut$ and $Y = \mu_y = ylen_{tot}/2$ denote the real-time horizontal location of pressure distribution as shown in Fig. 4.

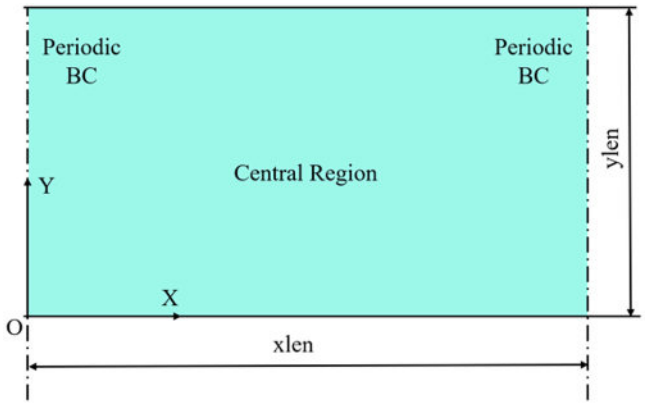

FIG. 2. HOS-Ocean domain.

During the solution phase, Fourier transforms are utilized in HOS-Ocean to compute derivative operators in spectral space. Differential operations are replaced by multiplicative manipulations [as shown in Eq. (21)], leading to a significant improvement in computational efficiency

$$\mathcal{F}\left[\frac{\partial f}{\partial x}\right] = ik_x\mathcal{F}[f], \quad \mathcal{F}\left[\frac{\partial f}{\partial y}\right] = ik_y\mathcal{F}[f]. \tag{21}$$

In addition, to mitigate numerical instability, a transition period is introduced in the free-surface boundary conditions through the use of a relaxation scheme, which enables a smooth progression from linear initial conditions to fully nonlinear computation. Further details on this approach can be found in Ref. 60. As shown in Fig. 5, the solution of the free-surface boundary conditions [Eqs. (3) and (4)] involves an iterative procedure for ϕ^s and η. In HOS-Ocean, an integrating factor proposed by Fructus *et al.*[61] is employed to appropriately transform the variables, enabling the linear part of the equations to be integrated analytically, while the nonlinear part is treated numerically. The time stepping for the iterative solution is performed using an adaptive-time-step, six-stage, fifth-order (fourth-order) Runge–Kutta method. This method estimates the current local truncation error by computing numerical solutions at two different orders (fifth and fourth). If the estimated error exceeds the prescribed tolerance, the procedure reduces the time step and recalculates the current step. When the error falls within the acceptable range, the current step is accepted, and the next time step is predicted and adjusted based on both the error magnitude and a safety factor. This strategy enhances computational efficiency while maintaining accuracy. The step size correction factor is constrained within reasonable bounds, preventing excessive growth or reduction of the time step. The adaptive time step is stringently constrained to the minimum value among three critical parameters: the computationally optimized step from error estimation, the prescribed output interval, and the stability limit imposed by the linear component of the model. This triple safeguard mechanism provides a comprehensive safeguard for numerical precision and computational stability throughout the simulation. For further details, refer to Ref. 30.

III. RESULTS AND DISCUSSION

A. Numerical verification and validation

To evaluate the computational capability of HOS-Ocean in simulating ship wakes with the introduction of a moving pressure distribution term, calculations are performed for $Fr = 0.414$ at a water depth of 171 m (under deep-water conditions where results become insensitive to water depth). The symbol Fr is the Froude number based on ship length L_s,

$$Fr = \frac{U}{\sqrt{gL_s}}. \tag{22}$$

Referring to the pressure distribution model established by Lo,[23] the parameter β is set to 8, corresponding to a contour level of e^{-2} relative to the peak value for characterizing the hull length and beam. Using the DTMB 5415 as the reference hull form—with a length of 142.0 m, beam of 18.9 m, and draft of 6.16 m—the shape of the pressure distribution function is determined via Eq. (20). As depicted in Figs. 6(b) and 6(c), the frontal and profile views both show a Gaussian-type pressure distribution symmetric about the origin, where the pressure peak occurs. Figure 6(a) reveals an elliptical footprint in the top-view plane, exhibiting smooth fore-aft transitions unlike the abrupt geometric

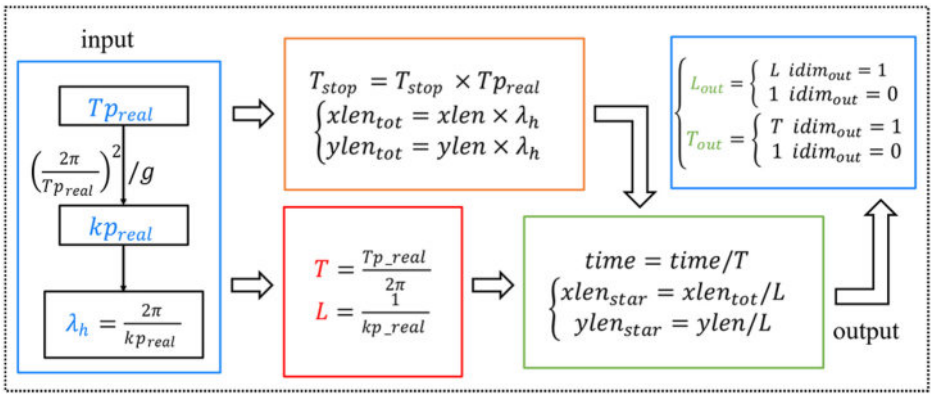

FIG. 3. Dimensionless processing procedure.

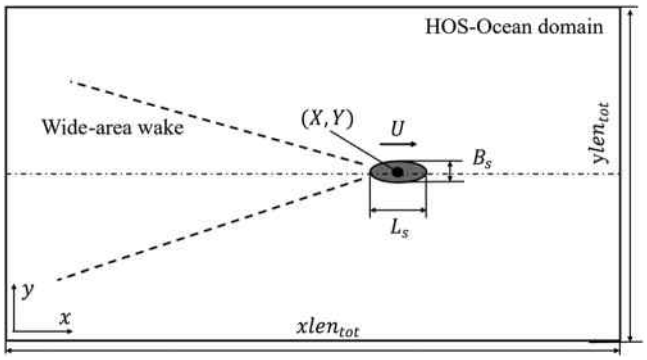

FIG. 4. Schematic diagram of the pressure distribution location.

changes typical of actual ship bows and sterns. The three-dimensional representation of the pressure distribution is provided in Fig. 7.

First, a study on grid convergence is conducted. To accommodate the moving pressure distribution defined over the computational grid, the domain size must be sufficiently large to prevent the distribution from exiting the boundaries. Moreover, as HOS-Ocean utilizes periodic boundary conditions, employing a domain with adequate transverse extent also helps mitigate periodicity-induced artifacts in the simulated wake. For this case, the order of HOS is $M = 3$, and the dimensionless parameters in Fig. 3 are set as follows: $xlen = 45$, $ylen = 20$, $Tp_{real} = 10$, and $T_{stop} = 45$. On this basis, five sets of grids are set up, and the number of grid nodes n_1 and n_2 in the x and y directions are shown in Table I. The row labeled "Time" indicates the actual computational time consumed, and the computing device features a 3.60 GHz Intel Core i7-9700 single-core processor. The

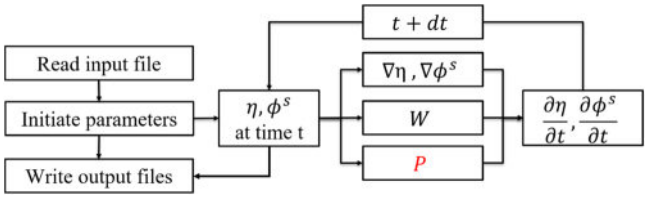

FIG. 5. Solving procedure in wake solver.

parameter η represents the free-surface elevation at the first wave peak ($x = 118$ m) along the transverse section located 46 m from the centerline. The relative errors between results obtained with successively refined grid resolutions are provided.

Figure 8 shows the computational results, specifically the wave field corresponding to Result-4, and the wave pattern is consistent with the one from Lo. Within the same length range (800 m), four peaks and troughs are observed, indicating wavelengths that are broadly consistent with literature values. The scattering angle of the divergent wave conforms to the Kelvin angle. This preliminary qualitative analysis confirms the computational accuracy of the method employed in this paper. The elevation data of the free surface along the x axis at a distance of $y' = 46$ m from the pressure center was extracted. The entire data are translated to align the coordinate axes with the experimental setup.

As shown in Fig. 9, comparing results from different mesh configurations reveals that numerical outcomes gradually converge toward a stable value as the number of meshes increases. It is observed that in HOS-Ocean, coarse meshes exhibit shorter computation times compared to fine meshes but appear to yield larger results. This discrepancy may stem from coarse meshes' less precise representation of pressure. When the grid configuration uses $n_1 = 128$ and $n_2 = 64$, this discrepancy is most pronounced. This finding suggests that, while dimensionalization in HOS-Ocean to some extent reduces the necessity for grid points, these points must still be determined with adequate caution. One can progressively refine the grid in order to address the limitations of coarse grids, as evidenced by the configurations that correspond to Result-2 and Result-3. Nevertheless, a small discrepancy still remains between these results and those obtained at convergence. However, if the objective is merely to expeditiously evaluate the qualitative plausibility of computational outcomes, such grid configurations may be sufficient. As the grid size is decreased to the configurations corresponding to Result-4 and Result-5, the results converge almost. As presented in Table I, the relative error is observed to be 7.3%. It is worth noting that the grid points in HOS-Ocean, based on a pseudo-spectral method, essentially correspond to frequency-domain discretization points.

Since Result-4 closely approximates Result-5 with less simulation time, Result-4 is considered for numerical validation. The result is compared with the experimental measurements from Lindenmuth *et al.*[64] and the numerical results from Gourlay.[65] In the near field, specifically near the first and second major wave crests, the computational

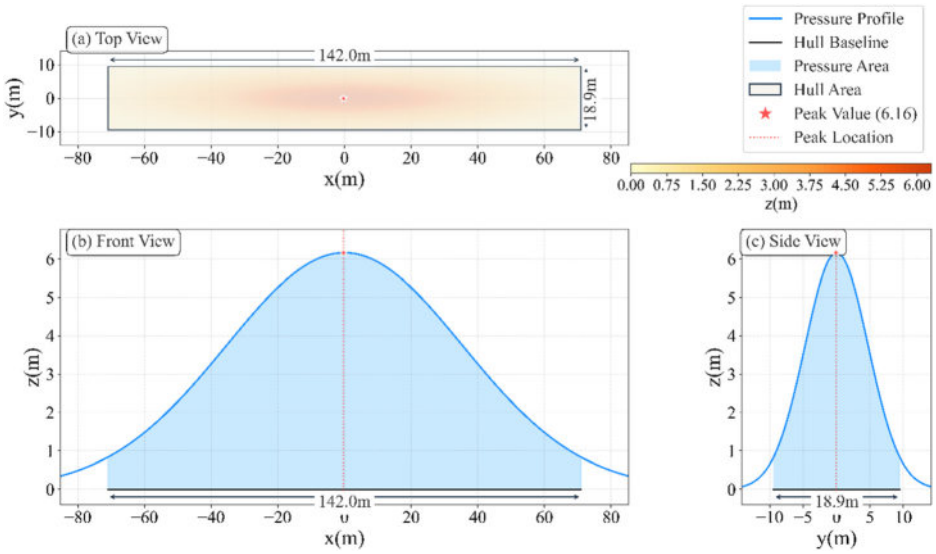

FIG. 6. Three-view diagram of pressure distribution, where $z = P/\rho g$.

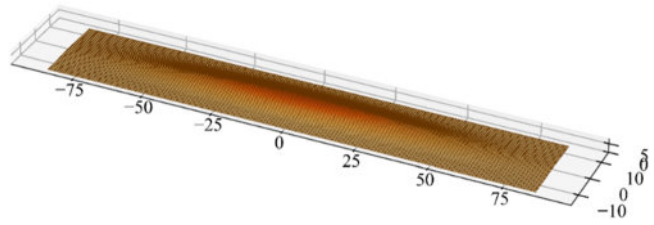

FIG. 7. Three-dimensional view of pressure distribution.

TABLE I. Grid convergence analysis: mesh configurations, computational expense, and resulting accuracy metrics.

	Result-1	Result-2	Result-3	Result-4	Result-5
n_1	128	180	256	360	512
n_2	64	100	128	200	256
Time/s	600	1500	3240	8040	16200
η/m	2.26	1.96	1.59	1.37	1.27
Error%	13.27	18.88	13.84	7.3	

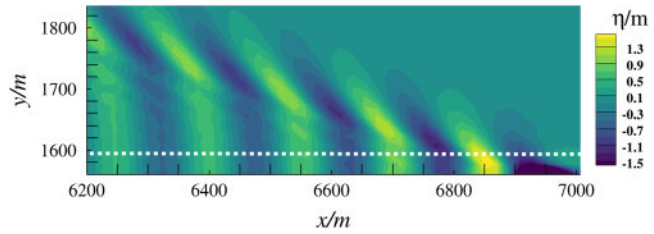

FIG. 8. The wave field predicted by the Gaussian pressure distribution for Result-4. The white dashed line marks the line $y' = 46$ m away from the centerline of the ship in HOS-Ocean domain.

results exhibit significant deviations. This is primarily due to discrepancies between the pressure distribution and the actual hull geometry. In the near field, the waves are primarily dominated by hull disturbances. However, elevation agreement is satisfactory in the far field. Overall, incorporating the moving pressure distribution term into HOS-Ocean enables the generation of reasonably accurate surface wake results (Fig. 10).

B. The effects of shape parameter β

It can be observed that the differences among the pressure distributions studied in Refs. 7, 23, and 24 fundamentally stem from the choice of the contour level defined relative to the peak value of the

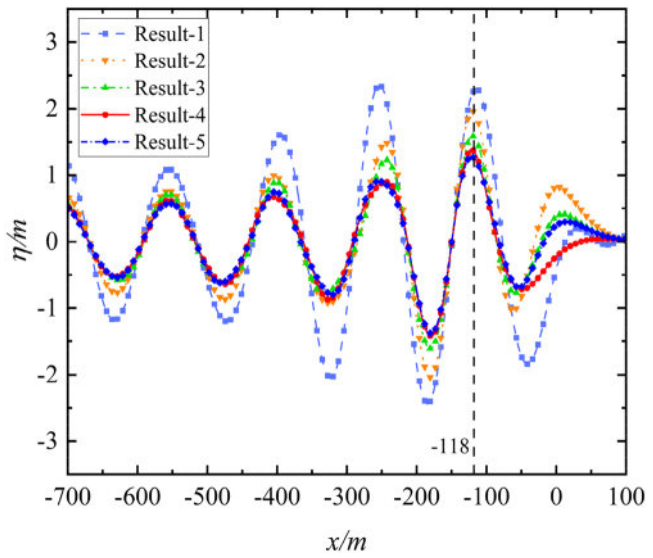

FIG. 9. Verification for grid convergence.

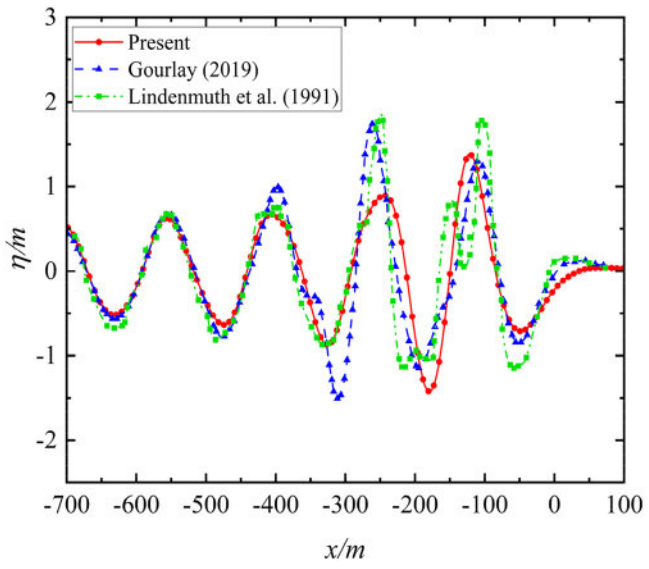

FIG. 10. Validation for result.

shape factor, at which the hull dimensions are characterized. The values of Moisy and Rabaud,[7] Lo,[23] Paprota[24] for beta are π^2, $4\log(10)$, 8, respectively. In other words, they correspond to different proportions of the peak values. Since a is proportional to β, i.e., $a = e^{\beta/4}$, it can be known that the value of Moisy is the largest, followed by Paprota, and Lo is the smallest. Their curves are compared as shown in Fig. 11. For convenience, only the results along the x axis are displayed, i.e., $y = 0$, and $\mu_x = \mu_y = 0$. While all distributions maintain a peak value of 1, the pressure distribution employed by Lo exhibits the flattest profile among the compared cases. A larger value of β results in a steeper curve; similarly, a larger a also leads to a sharper distribution. This relationship is consistently reflected in the slope of the function.

From a statistical perspective, the symbols μ and σ in the Gaussian function represent the mean and standard deviation of the data, respectively, characterizing the distribution of the data. The standard deviation σ describes the "dispersion" of the data. A low σ value indicates data that is concentrated around the mean, with a rapid decline on both sides of the peak, resulting in a "sharp" curve.

TABLE II. Parameter configurations: shape parameter β and its equivalent peak factor a.

β	6.44	8	$4\log(10)$	π^2	11.98
a	5	7.39	10	11.79	20

Conversely, a high σ value signifies dispersed data, characterized by a gradual decline on both sides of the peak, leading to a "flat" curve. Thus, a larger standard deviation corresponds to a broader and flatter distribution, while a smaller one produces a narrower and steeper distribution.

The wakes corresponding to five different β values (as shown in Table II) were calculated, and the data at $y' = 46$ m were compared as well. The results are shown in Fig. 12, with Fig. 13 providing a local enlargement of the shaded area. It should be noted that a sharper pressure distribution imposes stricter requirements on the computational grid; compared to a flatter distribution, capturing such a profile accurately within the same domain generally demands a higher grid resolution. However, for the sake of convenience in discussion, the same grid configuration is used throughout.

The surface elevations in the far field are nearly uniform, but exhibit differences at the maximum wave crest and trough. As beta increases, the pressure profile steepens, causing this peak to grow. It can be observed that when taking one-fifth of the peak value, the peak difference is relatively large because the pressure distribution is flatter at this point, and the flow changes are relatively gradual. For Moisy and Rabaud,[7] Lo,[23] Paprota,[24] the results are very similar. For actual ship hulls, whose bows, sterns, and sides are relatively steep, selecting a larger beta value is more reasonable. However, it should be noted that HOS-Ocean employs a global Fourier transform; excessively large values can cause the curve transitions to become non-smooth, potentially leading to computational crashes.

Although researchers commonly employ Gaussian pressure distributions to approximate hull-induced surface disturbances using consistent functional forms, variations exist in the selection of the shape parameter β. Current literature predominantly presents the distribution expressions without substantiating the parameter selection methodology or comprehensively addressing its hydrodynamic implications. This study consequently investigates the fundamental role of this parameter, conducting preliminary comparative analysis of

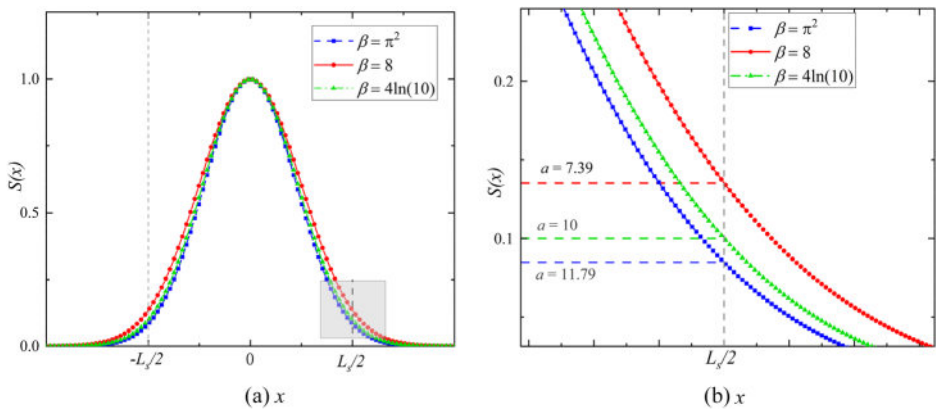

FIG. 11. Shape factor (x direction) corresponding to different beta values.

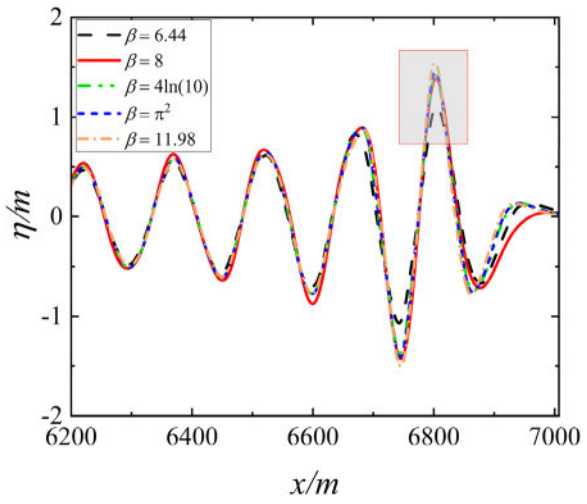

FIG. 12. η at $y' = 46$ m for different β.

representative β values (which exhibit relatively close numerical proximity). The results indicate that the variations in wake characteristics among these parameter configurations remain relatively modest within this range. Systematic investigation of β's influence requires methodical computation of wake patterns across progressively varying values (from minimal to substantial magnitudes), with detailed parametric analysis scheduled for subsequent research on improved pressure distribution models. Additionally, β exerts the same effect on both the x and y directions. To better approximate the actual hull, different beta values may be applied to the x and y directions, as shown in the following equation:

$$\frac{P(x-Ut,y)}{\rho} = \alpha \cdot e^{-\left[\beta_1 \cdot \frac{(x-X)^2}{L_s^2} + \beta_2 \cdot \frac{(y-Y)^2}{B_s^2}\right]}, \tag{23}$$

where β_1 and β_2 represent the shape coefficients in the x and y directions, respectively.

C. The HOS order M and usage of current

The impact of varying the order M in HOS-Ocean on the results is examined. Owing to the pseudo-spectral method employed in HOS-Ocean, Fourier transforms are frequently used, which can inevitably introduce aliasing effects. Aliasing errors arising from nonlinear products of order up to M in the pseudo-spectral procedure were systematically addressed by applying zero-padding in the spectral domain. The number of collocation points was extended following the half-rule to fully eliminate aliasing effects. To address this, a de-aliasing parameter p is incorporated into the model. For complete de-aliasing, it is optimal to set $p = M$; however, to reduce computational cost, a smaller value of p may be used to achieve partial de-aliasing.[30] The p-value must not exceed M. Considering that first-order de-aliasing may be inadequate to guarantee numerical accuracy, this study performs simulations only for orders $M > 1$. Full de-aliasing (i.e., $p = M$) is applied for $M = 2, 3$. For higher orders ($M = 4, 5$), a partial de-aliasing scheme with $p = 3$ is adopted to maintain computational efficiency. The actual computation time increases significantly with the order M. The results are shown in Fig. 14. The order M has little effect on the results, with outcomes for different orders being very close. Balancing computational accuracy and efficiency, an order of $M = 3$ meets the requirements.

When using a moving pressure distribution in HOS-Ocean, the required computational domain size increases proportionally with both the moving speed and the simulation duration. Higher speeds or longer simulation times necessitate a larger domain. To maintain accuracy, the number of grid points must also be increased accordingly, leading to higher computational cost. In addition, it requires a certain amount of time for the wake to reach a stable state. In the context of a moving pressure distribution, this distance cannot be overlooked. To mitigate this, an equivalent inflow condition is considered: as illustrated in Fig. 15, the pressure distribution is placed at a distance of two

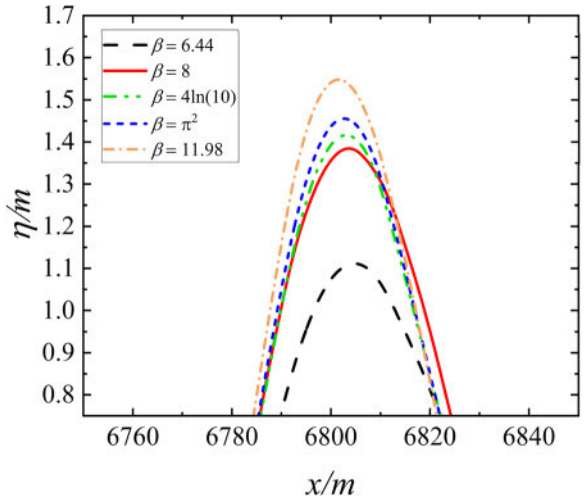

FIG. 13. The shaded area from Fig. 12.

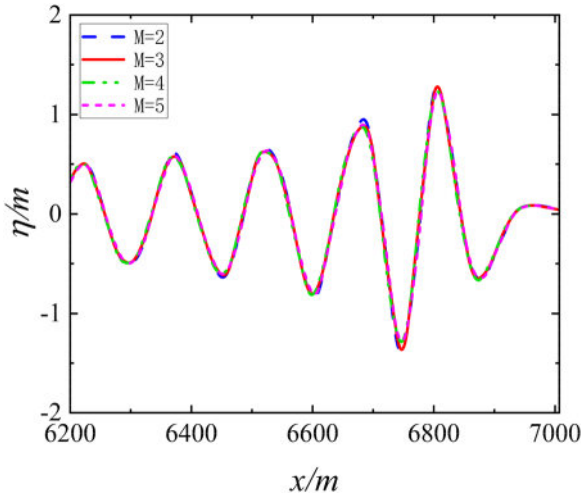

FIG. 14. Surface elevation for different orders.

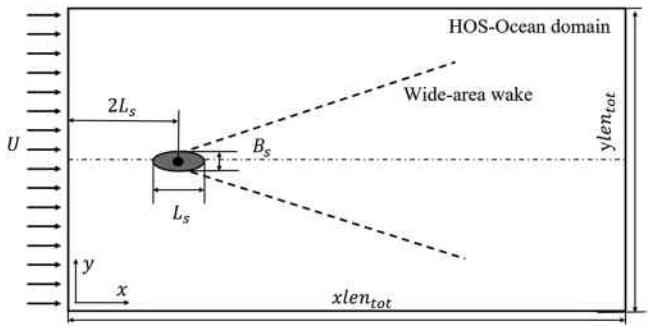

FIG. 15. HOS-Ocean domain within a constant flow velocity.

ship lengths $2L_s$ from the left boundary, with the inflow velocity set equal to the ship velocity U. Furthermore, prolonged simulations may introduce interference from periodic boundary conditions on the Kelvin wake, necessitating a constraint on the minimum domain size to avoid such artifacts. This constraint is intrinsically linked to the vessel's velocity and the total simulation duration. To determine the lower bound of the domain size, the wedge-shaped region of the wake is considered. Starting from the apparent wake angle θ_{apparent}, the geometric condition is adopted

$$\tan\left(\theta_{\text{apparent}}\right) \approx \frac{ylen_{tot}}{2 \cdot xlen_{tot}}. \tag{24}$$

Considering that a transition period T_{pre} of 80–100 s is required in HOS-Ocean for the Kelvin wake to develop after introducing the pressure distribution, the required domain length can be estimated based on the total simulation time T_{tot} and the wave propagation distance. The longitudinal domain size should satisfy

$$xlen_{tot} \approx 1.5L_s + \left(T_{\text{tot}} - T_{\text{pre}}\right) \cdot U, \tag{25}$$

where L_s denotes the ship length and U the ship speed. Thus, by combining Eqs. (24) and (25), the appropriate computational domain size or simulation duration can be rationally determined to mitigate the influence of periodic boundary conditions, based on θ_{apparent}. Here, θ_{apparent} can be selected according to the water depth h and navigation velocity U, such as the classical Kelvin wake angle of 19.28° under deep-water conditions. It should be noted that this formulation neglects viscous effects, implicitly assuming the Kelvin wake can propagate indefinitely without attenuation. A more refined approach would require incorporating viscous terms into the free-surface boundary conditions, which lies beyond the scope of this study.

Due to the symmetry of the pressure distribution, its fore and aft sections are identical, thus eliminating the need to adjust the bow direction as would be required for a real vessel. A comparative analysis of the results obtained using this approach is presented in Fig. 16. The result obtained using current are comparable to the one within moving pressure, indicating that substituting current for moving pressure distribution in HOS-Ocean is reasonable. In subsequent wide-area wake numerical simulations, current will be utilized as an equivalent substitute.

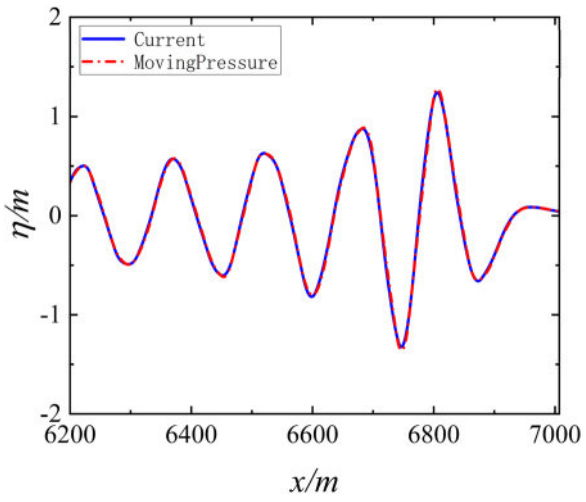

FIG. 16. Comparison of current and moving pressure.

D. Kelvin wake at different Froude number Fr and sailing angle θ

The Kelvin wakes corresponding to different Froude numbers and different sailing angles were calculated. Perform a two-dimensional, discrete Fourier transform on the free-surface elevation of the wake at steady state. The general form is as follows:

$$\eta\left(f_x, f_y\right) = \Delta x \Delta y \sum_{n=0}^{N-1} \sum_{m=0}^{M-1} \eta(m,n) e^{-i2\pi(ml/M + nk/N)}, \tag{26}$$

$$f_x = \frac{l}{M\Delta x} \quad (l = 0, 1, \ldots, M-1), \tag{27}$$

$$f_y = \frac{k}{N\Delta y} \quad (k = 0, 1, \ldots, N-1). \tag{28}$$

The 2D power spectral density (2D-PSD) can be expressed as Eq. (26) multiplied by a coefficient

$$\left|PSD\left(f_x, f_y\right)\right| = \frac{\Delta x \Delta y}{MN} \left| \sum_{n=0}^{N-1} \sum_{m=0}^{M-1} \eta(m,n) e^{-i2\pi(ml/M + nk/N)} \right|^2, \tag{29}$$

where M and N represent the discrete values of the free-surface elevation in the x and y directions, respectively. Δx and Δy denote the sampling intervals, while l and k are the indices in the x and y directions, respectively. f_x and f_y are the spatial frequencies in the x and y directions, respectively. Multiplying them by 2π yields the spatial wave numbers k_x and k_y.

Consider the linear dispersion relation in infinite water depth, i.e.,

$$\omega^2 = gk, \tag{30}$$

where ω is the angular frequency, $k = \sqrt{k_x^2 + k_y^2}$ denotes the wavenumber. According to the Doppler effect, when the ship travels along the positive x axis at velocity U in the reference frame, then

$$\omega' = \omega - Uk_x. \tag{31}$$

Under the assumption that the Kelvin wake remains stationary relative to the vessel, i.e., $\omega' = 0$, combining Eqs. (30) and (31) yields,

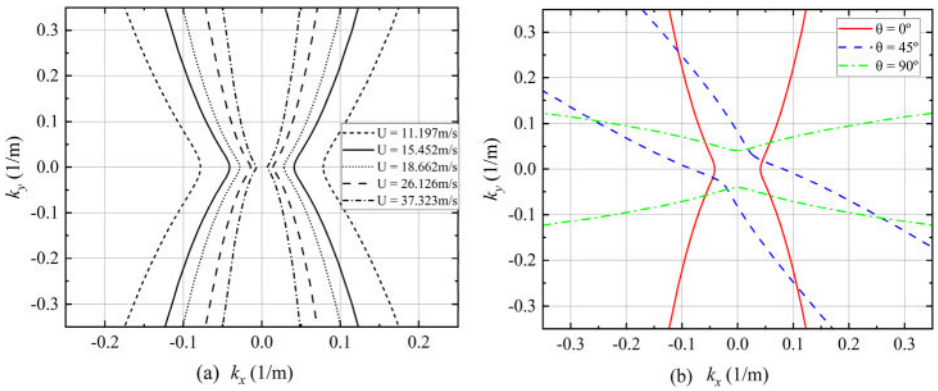

FIG. 17. Theoretical shape of the Kelvin wake pattern in the spectral domain. (a) The ship is assumed to be moving in positive x direction; and (b) a ship with a heading of θ counterclockwise with respect to the positive x axis, $U = 15.452\,\mathrm{m/s}$.

$\sqrt{gk} = Uk_x$ and $g\sqrt{k_x^2 + k_y^2} = (Uk_x)^2$, and then the dispersion relation follows that

$$k_y^2 = k_x^2\left(\frac{U^4}{g^2}k_x^2 - 1\right). \tag{32}$$

The curves for different U are shown in Fig. 17(a). When the ship sails at a certain angle to the x axis, such as 0°, 45°, and 90°, the theoretical dispersion relation curve is shown in Fig. 17(b).

The dispersion relation specifies the condition that the wavenumber components k_x and k_y must satisfy for Kelvin waves to form behind a uniformly moving object. It explains why ship waves are confined within a V-shaped sector. When k_x becomes sufficiently large, the term $U^4k_x^2/g^2$ dominates, leading to $k_y \propto U^2k_x^2$. This indicates that k_y increases quadratically with k_x, resulting in short wavelengths perpendicular to the direction of motion and wave crests nearly aligned with the ship's trajectory. Such short waves are typically influenced by surface tension, which falls beyond the scope of this dispersion relation.

Setting $k_y = 0$ yields the cutoff wavenumber $k_x^c = g/U^2$, representing the minimum k_x required for ship wave formation. Only when $k_x \geq k_x^c$ does k_y^2 remain non-negative, allowing visible ship waves to develop. This implies that the maximum wavelength in the x direction is $\lambda_{x,\max} = 2\pi U^2/g$. Thus, higher ship speeds correspond to longer achievable wavelengths in the x direction.

As k_x approaches the cutoff wavenumber k_x^c, the term $(U^4k_x^2/g^2 - 1)$ tends to zero, causing $k_y \to 0$. This indicates that the wave component along the y-direction diminishes, and the wave propagates almost entirely along the x axis (the ship's direction), corresponding to the transverse wave system.

Furthermore, when the ship's speed U increases significantly, k_x^c approaches zero. This implies that the minimum k_x required for ship waves becomes very small, allowing waves with extremely long wavelengths (i.e., very small k_x) to develop in the x direction. Consequently, waves generated by high-speed vessels can extend over considerable distances. Under such conditions, the term $U^4k_x^2/g^2$ again becomes dominant, leading to $k_y \propto U^2k_x^2$. As a result, the wave crests align increasingly with the ship's direction, and the wake system becomes notably narrow and elongated.

The wake results and power spectral density at different Froude numbers are shown in Fig. 18. All simulations employ identical computational grid configurations and durations. The solid red line corresponds to the Kelvin angle, while the dashed orange line represents the apparent wake angle. Bright regions indicate wave crests, and dark regions denote wave troughs. Consistent with classical Kelvin theory, the entire wake is confined within a wedge-shaped region. This wedge persists over a broad span, propagating several kilometers. As speed increases, the wake's dispersion distance also grows. Within an identical time duration, a wave system generated by a vessel with larger velocity covers a larger propagation distance.

When $Fr = 0.3$, the wake is predominantly composed of transverse waves (also referred to as bow waves), while divergent waves are hardly noticeable. Under this condition, the Kelvin angle θ_{Kelvin} and the apparent wake angle $\theta_{apparent}$ nearly coincide. As Fr increases, the transverse and divergent waves exhibit opposite trends: the divergent waves become increasingly pronounced and gradually dominate the wake structure. Until at $Fr > 0.7$, transverse waves are almost entirely absent. Throughout this process, the apparent wake angle $\theta_{apparent}$ progressively deviates from the Kelvin angle θ_{Kelvin} and continues to decrease with increasing Fr.

In the power spectral density plot, the white line represents the theoretical dispersion relation curve. At low Froude numbers, the power spectral density (PSD) is dominated by two distinct peaks corresponding to the cutoff wavenumbers of transverse waves, with negligible spectral energy associated with divergent waves. As Fr increases, a curved spectral component emerges and progressively organizes into a well-defined X-arm pattern, signifying the excitation of divergent waves. Concurrently, the separation $\Delta k_x = 2k_x^c$ between the spectral peaks decreases, indicating a monotonic reduction in the cutoff wavenumber k_x^c approaching zero. This evolution is accompanied by attenuation of spectral energy near the vertex region—consistent with the decay of transverse waves—and a redistribution of energy toward the developing arms as divergent waves become dominant. Furthermore, the included angle between the spectral arms increases systematically with Fr, in accordance with the corresponding decrease in the apparent wake angle $\theta_{apparent}$. This pattern of change is consistent with the theoretical representation shown in Fig. 17(a).

The apparent wake angle $\theta_{apparent}$ is preliminarily extracted. According to the theoretical formula for wake angle considering bow-stern wave interference from the referenced literature,[2,22,62] the expression is given as

$$\theta_{apparent} = \frac{\sqrt{\pi^2 Fr^4/l^2 - 1}}{2\pi^2 Fr^4/l^2 - 1}, \tag{33}$$

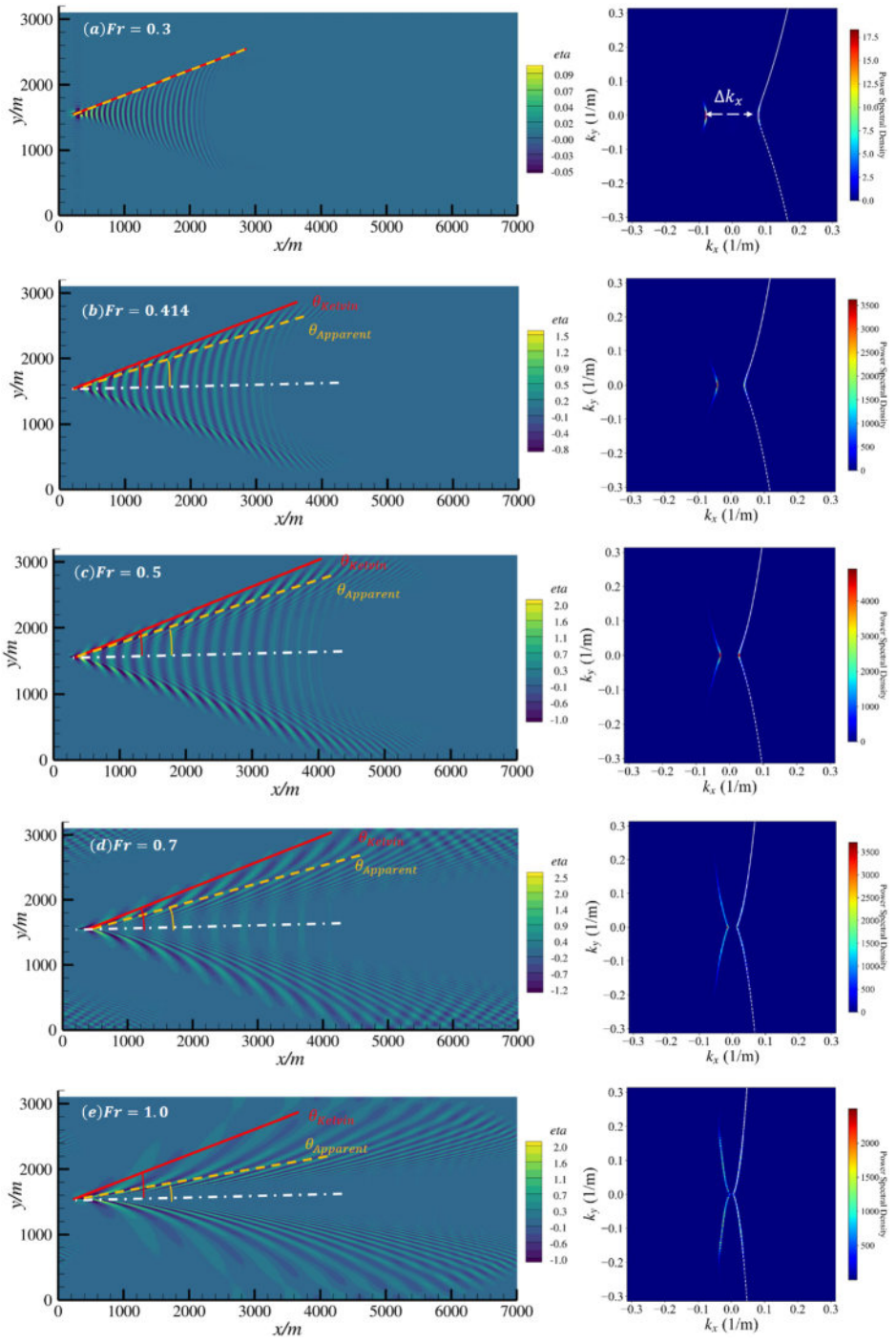

FIG. 18. Kelvin wake at different Froude number *Fr* from 0.3 to 1.0.

where l denotes the (non-dimensional) distance between the effective origins of the bow and stern waves. As illustrated in Fig. 19, theoretical curves of the wake angle are plotted for $l = 0.5$, 0.6, and 0.9. The wake angle profile produced by the Gaussian pressure distribution aligns closely with the theoretical curve corresponding to $l = 0.6$, indicating that the effective non-dimensional length represented by this pressure distribution is ∼0.6. Moreover, the results demonstrate that for a constant Froude number Fr, a reduction in the effective length l leads to a corresponding decrease in the observed wake angle $\theta_{apparent}$. This systematic variation underscores the sensitivity of the wake pattern to the spatial separation between the bow and stern-wave sources and provides a quantitative basis for evaluating the representational

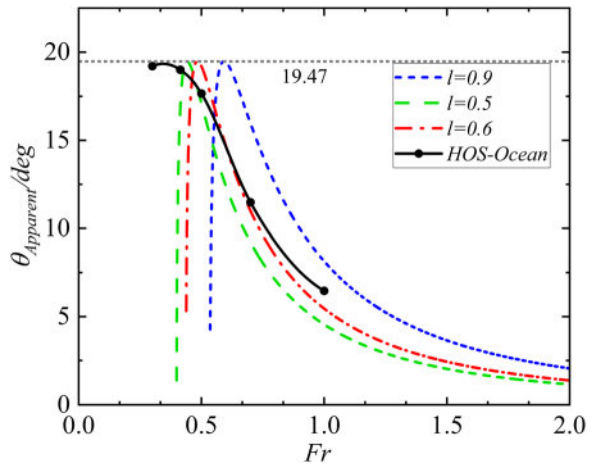

FIG. 19. Comparison of the apparent wake angle $\theta_{apparent}$ for different effective lengths l with HOS-Ocean results.

accuracy of the pressure distribution model in capturing hull-induced wave phenomena.

As illustrated in Fig. 20, the outcomes for heading angles of 45° and 90° are demonstrated. The direction of travel is indicated by the pink arrows. As is evident, the shape of the power spectral density undergoes a corresponding rotation, aligning with the pattern depicted in Fig. 17(b).

E. Kelvin wake at varied water depth h

Subsection III D discussed the relationship between the length-based Froude number and the ship wake. This subsection examines the variation of the Kelvin wake with water depth, introducing the depth-based Froude number, defined as $Fr_h = U/\sqrt{gh}$, where h represents the water depth. The relationship between these two Froude numbers can be readily seen from the following equation:

$$Fr_h = Fr \cdot \sqrt{\frac{L_s}{h}}. \tag{34}$$

Since the water depth varies and may not satisfy the deep-water condition, it is necessary to consider the general form of the dispersion relation, which modifies Eq. (30) by introducing a coefficient, as shown in Eq. (35). Correspondingly, Eq. (32) is then changed to Eq. (36)

$$\omega^2 = gk \cdot \tanh(kh), \tag{35}$$

$$k_y^2 = k_x^2\left(\frac{U^4}{\left(g\tanh(kh)\right)^2}k_x^2 - 1\right). \tag{36}$$

Using polar coordinate transformation, with the wave vector magnitude k as the parameter and φ as the angle between the wave vector and the k_x axis

$$\begin{cases} k_x = k\cos\varphi, \\ k_y = k\sin\varphi, \end{cases} \tag{37}$$

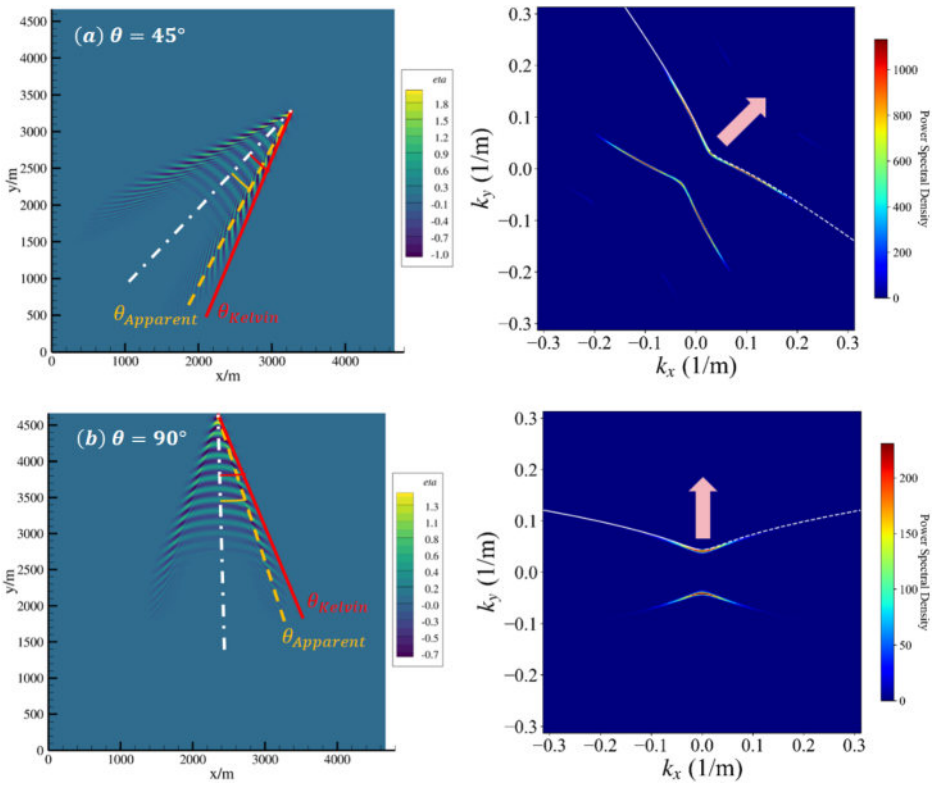

FIG. 20. Wake at heading angles of 45° and 90°.

TABLE III. Water depth-related parameters.

h(m)	Fr_h	λ(m)	h/λ
25	0.9867	130.38	0.192
30	0.9007	137.30	0.218
35	0.8339	142.49	0.246
50	0.6977	151.29	0.330

$$\cos^2\varphi = \frac{g\tanh(kh)}{U^2 k}. \tag{38}$$

Let $tmp = \frac{g\tanh(kh)}{U^2 k}$, and it is evident that the condition $0 \le tmp \le 1$ must be satisfied in order to ensure that $\cos^2\varphi$ lies within the specified interval $[0, 1]$. For each value of k that satisfies this condition, the corresponding value of $\cos\varphi$ and $\sin\varphi$ can be computed. Ultimately, the nonlinear dispersion relation can be expressed as follows:

$$\begin{cases} k_x^2 = k^2 \cdot tmp, \\ k_y^2 = k^2 \cdot (1 - tmp). \end{cases} \tag{39}$$

The wake at varying water depths was calculated for $Fr = 0.414$, with the relevant parameters displayed in Table III, where $\lambda = \frac{gT^2}{2\pi}\tanh(kh)$ denotes wavelength. The theoretical dispersion relation curve is shown in Fig. 21.

Additionally, let $\xi = kh$, after substituting Fr_h into tmp, one can obtain $\frac{\tanh(\xi)}{Fr_h^2 \xi} \le 1$, and the cutoff wave number for the nonlinear dispersion relation can be written as $k_x^c = \frac{g}{U^2}\tanh(\xi)$. For the deep-water condition, the cutoff wave number can be written as a function of Fr, i.e., $k_x^c = \frac{1}{Fr^2 L}$. As demonstrated in Fig. 22(a), the initial decrease in k_x^c is rapid as Fr increases. However, when Fr exceeds 0.3, the rate of decrease slows down and the value of k_x^c gradually approaches zero. At $Fr = 1$, the result is almost zero. The patterns illustrated in Figs. 17(a) and 18 are consistent with this behavior. In addition, as depicted in Fig. 22(b), when $Fr_h < 0.6$, k_x^c approaches the cutoff wavenumber $g/U2$ corresponding to the deep-water dispersion relation. As the water depth decreases, the k_x^c simultaneously diminishes. It is evident that this trend undergoes a substantial acceleration when $Fr_h < 0.9$, accompanied by a rapid decline in k_x^c until it attains a value of zero when $Fr_h \ge 1$. As illustrated in Figs. 21 and 23, this pattern is demonstrated from both theoretical and numerical perspectives.

The computational results are presented in Fig. 23, where the right column shows the power spectral density, with the red and white curves representing the theoretical dispersion relations for nonlinear and linear cases, respectively. All calculated Froude numbers Fr_h are less than 1.0. Within this Froude number range, the compositional structure of the Kelvin wake remains unchanged compared to the deep-water case, still consisting of transverse and divergent waves. However, as Fr_h increases, i.e., as the water depth h decreases, the included angle between the two arms of the Kelvin wake gradually widens. At $Fr_h = 0.6977$, corresponding to a relative water depth

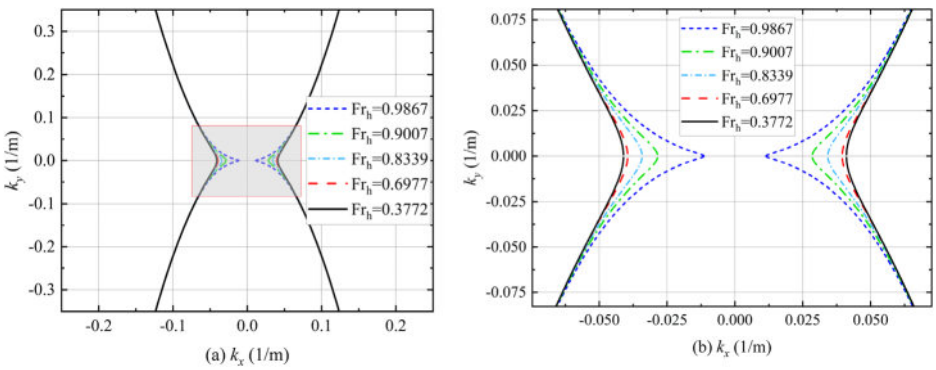

FIG. 21. Theoretical shape of the Kelvin wake pattern at different Fr_h in the spectral domain.

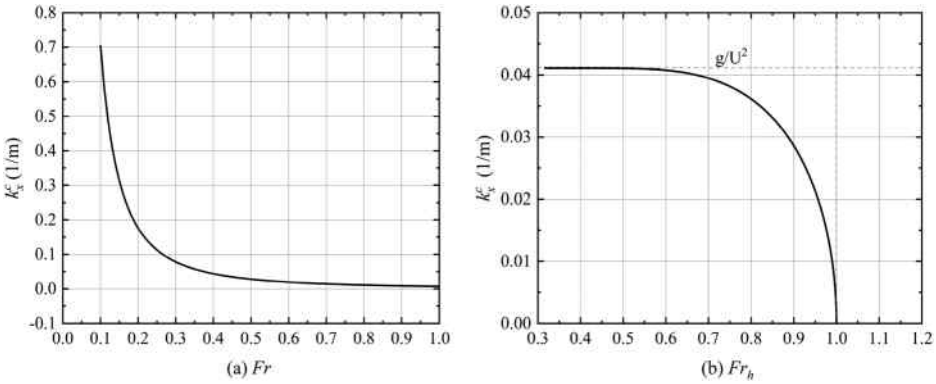

FIG. 22. Cutoff wavenumber k_x^c for different Foude numbers. (a) Varies with sailing speed U. (b) Varies with water depth h.

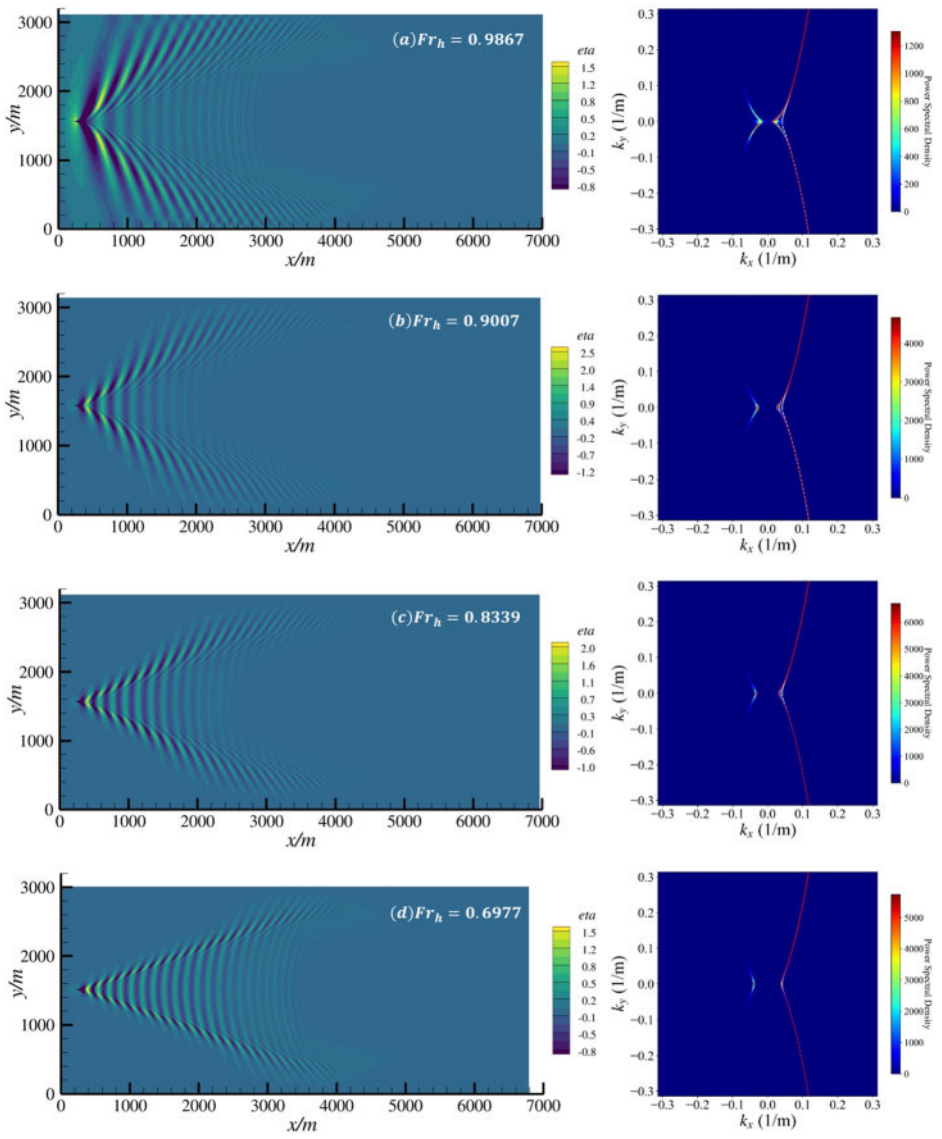

FIG. 23. Kelvin wake at different Froude number Fr_h (water depth h).

$h/\lambda = 0.33$, the overall waveform closely resembles that under deep-water conditions. Furthermore, the dispersion relation curves derived from the power spectral density show strong agreement with the theoretical nonlinear dispersion relation, while deviations from the linear theory occur at the cutoff wavenumber k_x^c, where the actual value is smaller and approximately proportional to the water depth.

F. Kelvin wake in the presence of environmental waves

The HOS-Ocean model is designed to simulate large-scale nonlinear waves, including irregular waves. This section is a progression on from the preceding foundation, with the objective of simulating Kelvin wakes in a random wave environment. In this manner, an initial examination is provided of how the external environment affects the wake. In the extant open-source HOS-ocean model, the sole available wave spectrum is the JONSWAP spectrum. The project was formally designated the Joint North Sea Wave Project (JONSWAP) and was first mooted in 1969. The spectral density function $S(\omega)$ for the JONSWAP spectrum can be expressed as

$$F_J(\omega) = C_J \omega^{-5} \exp\left(-\frac{5}{4\omega^4}\right) \gamma^{\exp\left[-\frac{(\omega-1)^2}{2\sigma^2}\right]}, \tag{40}$$

$$C_J = 3.279E, \quad \gamma = 3.3, \quad \sigma = \begin{cases} 0.07(\omega < 1), \\ 0.09(\omega \geq 1). \end{cases} \tag{41}$$

The spectral peak enhancement factor, denoted by γ, is conventionally set to 3.3. The symbol E denotes the energy density of the wave field, which can be estimated using the relationship $H_s = \sqrt{4E}$, where H_s is the significant wave height of that wave field. It is important to note

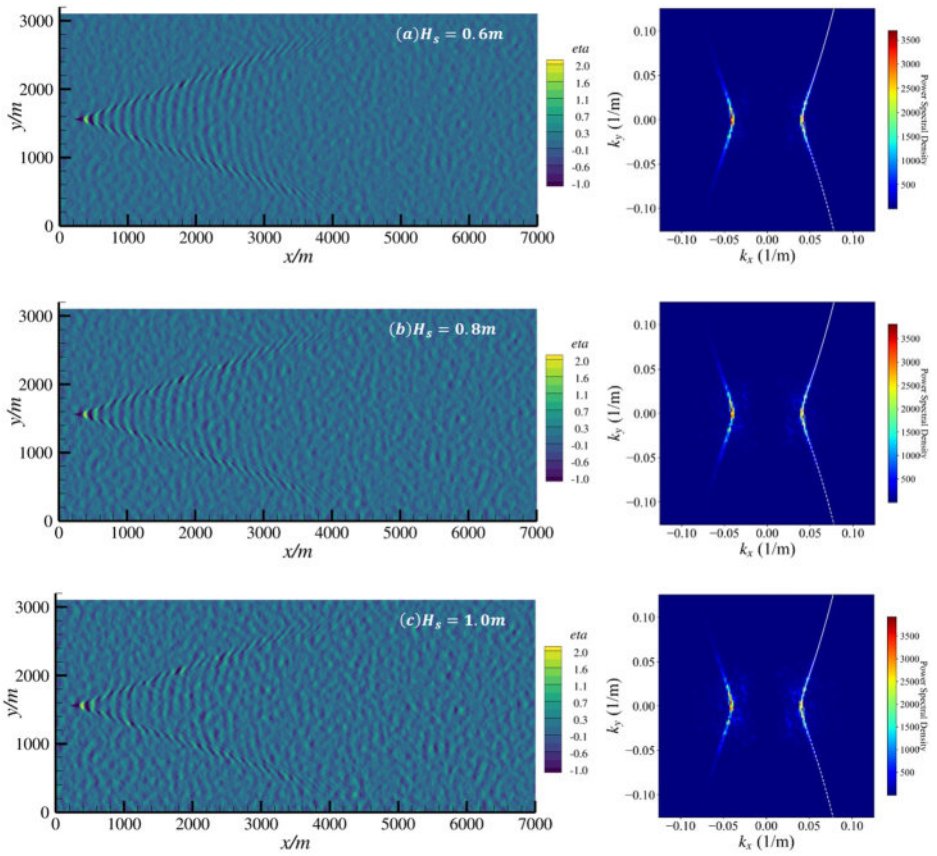

FIG. 24. Kelvin wake in the presence of environmental wave, e.g., random wave.

that Eq. (41) represents a normalized spectral density function, where both the peak frequency ω_p corresponding to the spectral peak, and the gravitational acceleration g, are set to 1.

Taking the spectral peak period $Tp_{real} = 10$ s, $Fr = 0.414$ for the deep-water condition, the Kelvin wake under random wave conditions was calculated for a range of significant wave heights, $H_s = 0.6,\ 0.8,$ and 1.0 m. For the purposes of facilitating discussion, the selection of wave random phases is fixed at the grid nodes. This means that identical grid random phase seeds yield consistent results. In order to ensure reproducibility, this seed remains unchanged for each simulation run. The results are presented in Fig. 24. In the presence of environmental waves, Kelvin wakes become relatively less distinct, particularly in the far field where transverse waves, which are comparable in amplitude to environmental waves, become nearly indistinguishable. The random waves manifest in the power spectrum as scattered points near the dispersion relation curve. These points become increasingly prominent across the spectrum as significant wave height H_s increases, which means that they exert varying degrees of influence on Kelvin wakes.

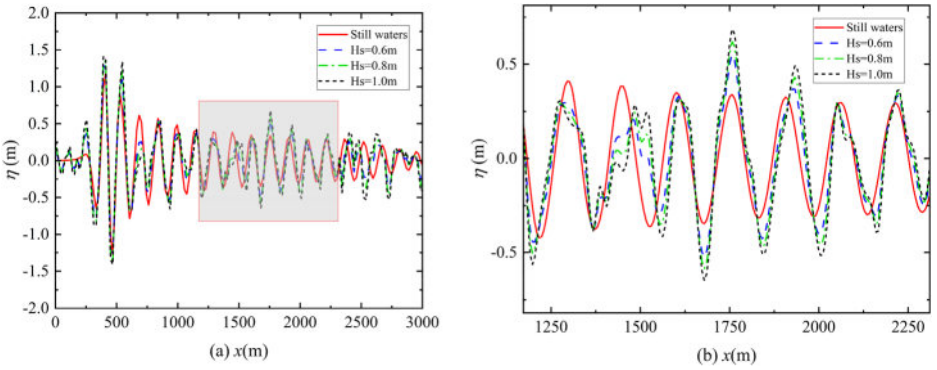

FIG. 25. Surface elevation at $y' = 46$ m away from the centerline.

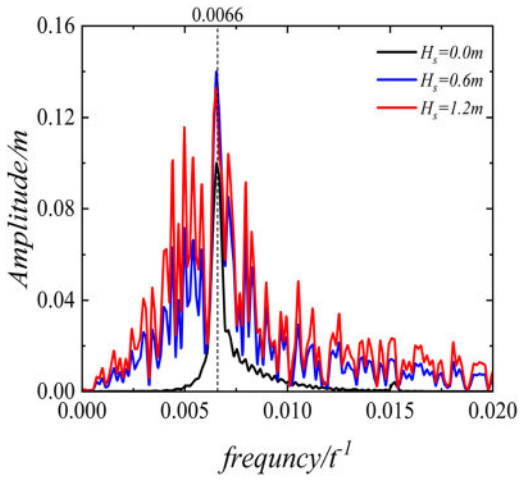

FIG. 26. Spectral analysis: η at $y' = 46$ m away from centerline.

Random wavefronts are regarded as the superposition of a finite number of harmonic components, which satisfy a Gaussian distribution model. Therefore, the elevation of the wavefront at time t can be expressed as follows:

$$\eta_r(x,y,t) = \sum_{m=1}^{M}\sum_{n=1}^{N} a_{mn}\cos\left(k_m^r x + \mathrm{k_n^r} y - \omega_{mn} t + \chi_{mn}\right). \quad (42)$$

In the given Eq. (42), the symbol a_{mn} represents the amplitude corresponding to each wavenumber $k^r = \sqrt{(k_m^r)^2 + (k_n^r)^2}$, ω_{mn} denotes the corresponding frequency, which satisfies the dispersion relation, and the phase χ_{mn} follows a uniform distribution between 0 and π. Ultimately, the superposition of the environmental wave and the free-surface elevation of the Kelvin wake yields

$$\eta_{tot} = \eta_{Kelvin} + \eta_r. \quad (43)$$

As shown in Fig. 25, the elevation profile at a transverse distance of y' = 46 m from the centerline is presented. The random ocean waves introduce stochastic interference with the Kelvin wake. When constructive interference occurs, the wave elevation increases, making the wake more pronounced, whereas destructive interference reduces the elevation and renders the wake less discernible. In general, the presence of ambient waves reduces the detectability of the Kelvin wake. For all the different significant wave heights H_s considered in the computations, the same random phase χ_{mn} is applied, resulting in consistent waveform characteristics. The intensity of interference with the Kelvin wake scales with the significant wave height, where higher significant wave heights induce more pronounced interference effects from the random waves. Furthermore, due to the irregular nature of the random waves, the peaks and troughs of the wake may become less regular, as observed in the wave crest at $x = 1500$ m.

A preliminary spectral analysis was conducted on the longitudinal free-surface elevation recorded at a transverse offset of 46 m from the centerline. The results, presented in Fig. 26, compare the case with no ambient waves ($H_s = 0$ m) to that with a superimposed random wave field. In the absence of ambient waves, the spectrum of the Kelvin wake is dominated by a sharp peak near 0.0066 Hz, with minimal energy distributed outside this narrow band. When ambient waves are present, the spectral peak becomes more pronounced, and the energy distribution broadens significantly, exhibiting increased contributions across both lower- and higher-frequency ranges.

This section of the study aims to provide a preliminary investigation into the capability of the open-source software HOS-Ocean for generating Kelvin wakes through introduced pressure distribution in the presence of ambient waves. The analysis presented here is intentionally preliminary and qualitative, serving as an initial reference for further studies on Kelvin wake generation in the presence of environmental waves. More in-depth and quantitative explorations are reserved for subsequent research.

IV. CONCLUSIONS

Based on the high-order spectral (HOS) method implemented in the open-source solver HOS-Ocean, this study simulates ship-generated surface wakes by introducing a moving pressure distribution into the dynamic free-surface boundary condition. This approach efficiently captures wide-area wake patterns with significantly reduced computational cost. Quantitative validation against experimental measurements confirms the accuracy and reliability of the numerical results.

The influence of the shape factor coefficient β on the pressure distribution was investigated: while larger values of β are recommended for realistic hull representation, excessively high values should be avoided in HOS-Ocean to ensure numerical stability. A third-order HOS truncation was found to provide an optimal balance between computational efficiency and accuracy. Furthermore, the equivalence between a moving pressure distribution and a stationary pressure field under inflow conditions was numerically demonstrated.

Analysis of wake patterns and power spectral density distributions across various Froude numbers (Fr and $\mathrm{Fr_h}$) qualitatively validates the proposed methodology. Furthermore, the presence of different Kelvin wakes and power spectral densities corresponding to varying speeds and water depths indicates the potential exposure of navigation parameters and the necessity of conducting wide-area wake calculations. Preliminary investigations suggest that Kelvin wakes become more difficult to detect in the presence of environmental waves, such as random waves. It should be emphasized that the current Kelvin wake simulation model is developed within the potential flow framework using the High-order spectral method, primarily applicable to wave conditions with low steepness. While the model demonstrates good capability in capturing the overall structure and far-field characteristics of Kelvin wakes, it cannot resolve strongly nonlinear phenomena such as stern-wave breaking, rooster tail formation, and viscous roll-up effects. The model's constraints originate in two fundamental assumptions: first, the inviscid and irrotational hypothesis breaks down under conditions involving free-surface reconnection and air entrapment; second, the exclusion of viscous forces precludes adequate representation of associated energy dissipation mechanisms.[66] Future investigations will consider incorporating viscous correction terms to address these physical processes.

In short, this work establishes an efficient and reliable framework for large-scale wake simulation, offering practical value for the prediction and analysis of ship wakes in real-world applications.

In the future, the pressure distribution model can be further improved to more accurately characterize the disturbance of the actual ship hull on the free surface. In addition to approximating hull geometry using predefined mathematical equations, external realistic hull

data [e.g., from Computer-Aided Design (CAD) models or CFD results] can be introduced and processed to better represent the ship body, thereby achieving higher precision in wake simulation. While direct application of discrete hull surface data would theoretically provide optimal accuracy, this approach introduces significant implementation challenges. The fundamental requirement for unique pressure mapping at each (x, y) coordinate becomes problematic with complex hull geometries such as bulbous bows, where non-unique vertical mappings occur. Furthermore, capturing localized steep curvature would necessitate substantial grid refinement. However, since the HOS-Ocean model employs a global Fourier transform, it currently does not support local grid refinement in the pressure area, making it difficult to capture sharply varying pressure distributions. Is it feasible to implement local mesh refinement to further enhance computational efficiency? While this may be challenging to achieve within the high-order spectral (HOS) framework alone, hybrid approaches—such as viscous-potential flow coupling strategies[67–73]—could offer a viable solution.

ACKNOWLEDGMENTS

This work was supported by the National Natural Science Foundation of China (Grant Nos. 52201372 and 52131102), to which the authors are most grateful.

AUTHOR DECLARATIONS

Conflict of Interest

The authors have no conflicts to disclose.

Author Contributions

Pengju Bao: Data curation (equal); Formal analysis (equal); Investigation (equal); Visualization (equal); Writing – original draft (equal). **Mingxing Ren:** Investigation (equal); Methodology (equal); Resources (equal); Visualization (equal). **Fenglai Huang:** Conceptualization (equal); Methodology (equal); Resources (equal); Validation (equal). **Decheng Wan:** Conceptualization (equal); Funding acquisition (equal); Supervision (equal); Writing – review & editing (equal). **Yuan Zhuang:** Funding acquisition (equal); Resources (equal); Validation (equal); Writing – review & editing (equal).

DATA AVAILABILITY

The data that support the findings of this study are available from the corresponding author upon reasonable request.

REFERENCES

[1]L. Kelvin, "On ship waves," in *Popular Lectures and Addresses* (Macmillan, London, 1887), Vol. 111, p. 459.
[2]M. Rabaud and F. Moisy, "Ship wakes: Kelvin or Mach angle?" Phys. Rev. Lett. **110**(21), 214503 (2013).
[3]A. Darmon, M. Benzaquen, and E. Raphaël, "Kelvin wake pattern at large Froude numbers," J. Fluid Mech. **738**, R3 (2014).
[4]S. Miao and Y. Liu, "Wave pattern in the wake of an arbitrary moving surface pressure disturbance," Phys. Fluids **27**(12), 122102 (2015).
[5]R. Pethiyagoda, S. W. McCue, and T. J. Moroney, "What is the apparent angle of a Kelvin ship wave pattern?" J. Fluid Mech. **758**, 468–485 (2014).
[6]R. Pethiyagoda, T. J. Moroney, C. J. Lustri, and S. W. McCue, "Kelvin wake pattern at small Froude numbers," J. Fluid Mech. **915**, A126 (2021).
[7]F. Moisy and M. Rabaud, "Scaling of far-field wake angle of nonaxisymmetric pressure disturbance," Phys. Rev. E **89**, 063004 (2014).
[8]J. K. Tunaley, "The estimation of ship velocity from SAR imagery," in *IGARSS 2003: 2003 Proceedings of IEEE International Geoscience and Remote Sensing Symposium* (IEEE, 2003), Vol. 1, pp. 191–193.
[9]M. D. Graziano, M. D'Errico, and G. Rufino, "Ship heading and velocity analysis by wake detection in SAR images," Acta Astronaut. **128**, 72–82 (2016).
[10]I. Didenkulova, A. Sheremet, T. Torsvik, and T. Soomere, "Characteristic properties of different vessel wake signals," J. Coastal Res. **65**, 213–218 (2013).
[11]A. Sheremet, U. Gravois, and M. Tian, "Boat-wake statistics at jensen beach, florida," J. Waterw., Port, Coastal, Ocean Eng. **139**(4), 286–294 (2013).
[12]G. Benassai, V. Piscopo, and A. Scamardella, "Spectral analysis of waves produced by HSC for coastal management," J. Mar. Sci. Technol. **20**(3), 417–428 (2015).
[13]R. Pethiyagoda, S. W. McCue, and T. J. Moroney, "Spectrograms of ship wakes: Identifying linear and nonlinear wave signals," J. Fluid Mech. **811**, 189–209 (2017).
[14]A. Arnold-Bos, A. Martin, and A. Khenchaf, "Obtaining a ship's speed and direction from its Kelvin wake spectrum using stochastic matched filtering," in *2007 IEEE International Geoscience and Remote Sensing Symposium* (IEEE, 2007), pp. 1106–1109.
[15]G. Gomit, G. Rousseaux, L. Chatellier, D. Calluaud, and L. David, "Spectral analysis of ship waves in deep water from accurate measurements of the free surface elevation by optical methods," Phys. Fluids **26**(12), 122101 (2014).
[16]Y. X. Sun, P. Liu, and Y. Q. Jin, "Ship wake components: Isolation, reconstruction, and characteristics analysis in spectral, spatial, and TerraSAR-X image domains," IEEE Trans. Geosci. Remote Sens. **56**(7), 4209–4224 (2018).
[17]K. T. Dam, K. Tanimoto, and E. Fatimah, "Investigation of ship waves in a narrow channel," J. Mar. Sci. Technol. **13**(3), 223–230 (2008).
[18]L. Zaggia, G. Lorenzetti, G. Manfé, G. M. Scarpa, E. Molinaroli, K. E. Parnell, M. Gionta, and T. Soomere, "Fast shoreline erosion induced by ship wakes in a coastal lagoon: Field evidence and remote sensing analysis," PLoS One **12**(10), e0187210 (2017).
[19]G. M. Scarpa, L. Zaggia, G. Manfè, G. Lorenzetti, K. Parnell, T. Soomere, J. Rapaglia, and E. Molinaroli, "The effects of ship wakes in the Venice Lagoon and implications for the sustainability of shipping in coastal waters," Sci. Rep. **9**(1), 19014 (2019).
[20]L. C. Dempwolff, G. Melling, C. Windt, O. Lojek, T. Martin, I. Holzwarth, H. Bihs, and N. Goseberg, "Loads and effects of ship-generated, drawdown waves in confined waterways—A review of current knowledge and methods," J. Coastal Hydraul. Struct. **2**, 46–46 (2022).
[21]Z. Q. Zheng, L. Zou, and Z. J. Zou, "A numerical study of passing ship effects on a moored ship in confined waterways with new benchmark cases," Ocean Eng. **280**, 114643 (2023).
[22]J. He, C. Zhang, Y. Zhu, H. Wu, C. J. Yang, F. Noblesse, X. Gu, and W. Li, "Comparison of three simple models of Kelvin's ship wake," Eur. J. Mech. B **49**, 12–19 (2015).
[23]P. H. Y. Lo, "Approximate ship wake solution for fast computation," Ocean Eng. **235**, 109405 (2021).
[24]M. Paprota, "A Fourier Galerkin method for ship waves," Ocean Eng. **271**, 113796 (2023).
[25]P. Du *et al.*, "Simulation of ship maneuvering in a confined waterway using a nonlinear model based on optimization techniques," Ocean Eng. **142**, 194–203 (2017).
[26]P. Du *et al.*, "Resistance and wave characterizations of inland vessels in the fully-confined waterway," Ocean Eng. **210**, 107580 (2020).
[27]S. Ji, A. Ouahsine, H. Smaoui, and P. Sergent, "3D numerical modeling of sediment resuspension induced by the compounding effects of ship-generated waves and the ship propeller," J. Eng. Mech. **140**(6), 04014034 (2014).
[28]S. Kaidi, H. Smaoui, and P. Sergent, "Numerical estimation of bank-propeller-hull interaction effect on ship manoeuvring using CFD method," J. Hydrodyn. **29**(1), 154–167 (2017).
[29]D. G. Dommermuth and D. K. Yue, "A high-order spectral method for the study of nonlinear gravity waves," J. Fluid Mech. **184**, 267–288 (1987).
[30]G. Ducrozet, F. Bonnefoy, D. Le Touzé, and P. Ferrant, "HOS-ocean: Open-source solver for nonlinear waves in open ocean based on high-order spectral method," Comput. Phys. Commun. **203**, 245–254 (2016).

[31]C. Ma, Y. Zhu, H. Y. Wu *et al.*, "Wavelengths of the highest waves created by fast monohull ships or catamarans," Ocean Eng. **113**, 208–214 (2016).
[32]Y. Zhu, J. He, H. Wu *et al.*, "Basic models of farfield ship waves in shallow water," J. Ocean Eng. Sci. **3**(2), 109–126 (2018).
[33]C. Zhang, J. He, Y. Zhu *et al.*, "Interference effects on the Kelvin wake of a monohull ship represented via a continuous distribution of sources," Eur. J. Mech. B **51**, 27–36 (2015).
[34]J. He, C. Zhang, Y. Zhu *et al.*, "Interference effects on the Kelvin wake of a catamaran represented via a hull-surface distribution of sources," Eur. J. Mech. B **56**, 1–12 (2016).
[35]X. Chen, R. Zhu, Y. Song *et al.*, "An investigation on HOBEM in evaluating ship wave of high-speed displacement ship," J. Hydrodyn. **31**(3), 531–541 (2019).
[36]H. Behera and T. Sahoo, "Gravity wave interaction with porous structures in two-layer fluid," J. Eng. Math. **87**(1), 73–97 (2014).
[37]H. Behera, S. Koley, and T. Sahoo, "Wave transmission by partial porous structures in two-layer fluid," Eng. Anal. Boundary Elem. **58**, 58–78 (2015).
[38]L. J. Yiew *et al.*, "Wave-induced collisions of thin floating disks," Phys. Fluids **29**(12), 127102 (2017).
[39]L. J. Yiew *et al.*, "Hydrodynamic responses of a thin floating disk to regular waves," Ocean Modell. **97**, 52–64 (2016).
[40]G. K. Rajan, "Solutions of a comprehensive dispersion relation for waves at the elastic interface of two viscous fluids," Eur. J. Mech. B **89**, 241–258 (2021).
[41]G. K. Rajan, "Damping rate measurements and predictions for gravity waves in an air–oil–water system," Phys. Fluids **34**(2), 022113 (2022).
[42]H. Liang and X. Chen, "Viscous effects on the fundamental solution to ship waves," J. Fluid Mech. **879**, 744–774 (2019).
[43]L. V. LazauskasResistance, wave-making and wave-decay of thin ships, with emphasis on the effects of viscosity," Ph.D. thesis (Discipline of Applied Mathematics, School of Mathematical Sciences, University of Adelaide, 2009).
[44]L. Chen, G. He, A. Incecik, and D. Wang, "Comparative study on steady wave-making problem using viscous and potential-flow methods," Ocean Eng. **154**, 143–152 (2018).
[45]R. Brard, "Viscosity, "wake, and ship waves," J. Ship Res. **14**(04), 207–240 (1970).
[46]J. Kim, K. S. Kim, Y. C. Kim, S. H. Van, and H. C. Kim, "Comparison of potential and viscous methods for the nonlinear ship wave problem," Int. J. Nav. Archit. Ocean Eng. **3**(3), 159–173 (2011).
[47]E. Cumberbatch, "Effects of viscosity on ship waves," J. Fluid Mech. **23**(3), 471–479 (1965).
[48]W. Thomson, "I. On the waves produced by a single impulse in water of any depth, or in a dispersive medium," Proc. R. Soc. London **42**(251–257), 80–83 (1887).
[49]T. H. Havelock, "The propagation of groups of waves in dispersive media, with application to waves on water produced by a travelling disturbance," Proc. R. Soc. London, Ser. A **81**(549), 398–430 (1908).
[50]A. S. Peters, "A new treatment of the ship wave problem," Commun. Pure Appl. Math. **2**(2), 123–148 (1949).
[51]C. Chester, B. Friedman, and F. Ursell, "An extension of the method of steepest descents," Math. Proc. Cambridge Philos. Soc. **53**(3), 599–611 (1957).
[52]D. Q. Lu and A. T. Chwang, "Interfacial waves due to a singularity in a system of two semi-infinite fluids," Phys. Fluids **17**, 102107 (2005).
[53]D. Q. Lu and A. T. Chwang, "Interfacial viscous ship waves near the cusp lines," Wave Motion **44**(7–8), 563–572 (2007).
[54]Y. Z. Dai and M. Kashiwagi, "On the interfacial viscous ship waves pattern," in Proceeding of the 29th International Workshop on Water Waves and Floating Bodies, Osaka, Japan, 2014, pp. 25–28.
[55]H. Wu, J. He, Y. Zhu, and F. Noblesse, "The Kelvin–Havelock–Peters farfield approximation to ship waves," Eur. J. Mech. B **70**, 93–101 (2018).
[56]B. R. Seiffert and G. Ducrozet, "A comparative study of wave breaking models in a high-order spectral model," in *International Conference on Offshore Mechanics and Arctic Engineering* (American Society of Mechanical Engineers, 2017), Vol. 57748, p. V07BT06A050.
[57]B. R. Seiffert, G. Ducrozet, and F. Bonnefoy, "Simulation of breaking waves using the high-order spectral method with laboratory experiments: Wave-breaking onset," Ocean Modell. **119**, 94–104 (2017).
[58]B. R. Seiffert and G. Ducrozet, "Simulation of breaking waves using the high-order spectral method with laboratory experiments: Wave-breaking energy dissipation," Ocean Dyn. **68**(1), 65–89 (2018).
[59]V. E. Zakharov, "Stability of periodic waves of finite amplitude on the surface of a deep fluid," J. Appl. Mech. Tech. Phys. **9**(2), 190–194 (1968).
[60]D. Dommermuth, "The initialization of nonlinear waves using an adjustment scheme," Wave Motion **32**(4), 307–317 (2000).
[61]D. Fructus, D. Clamond, J. Grue, and Ø. Kristiansen, "An efficient model for three-dimensional surface wave simulations: Part I: Free space problems," J. Comput. Phys. **205**(2), 665–685 (2005).
[62]F. Noblesse, J. He, Y. Zhu, L. Hong, C. Zhang, R. Zhu, and C. Yang, "Why can ship wakes appear narrower than Kelvin's angle?," Eur. J. Mech. B **46**, 164–171 (2014).
[63]L. J. Doctors and S. D. Sharma, "The wave resistance of an air-cushion vehicle in steady and accelerated motion," J. Ship Res. **16**(04), 248–260 (1972).
[64]W. Lindenmuth, T. J. Ratcliffe, and A. M. Reed, "Comparative accuracy of numerical Kelvin wake code predictions-'Wake off," Report No. DTRC-91/004 (1991).
[65]T. P. Gourlay, "phFlow wavemaking calculations for the DTMB 5415 Hull," Perth Hydro Research Report No. **R2019-07** (2019).
[66]G. Ducrozet, F. Bonnefoy, and Y. Perignon, "Applicability and limitations of highly non-linear potential flow solvers in the context of water waves," Ocean Eng. **142**, 233–244 (2017).
[67]I. Gatin, V. Vukčević, and H. Jasak, "Coupling of higher order spectral method and computational fluid dynamics," in Proceedings of the 22th Symposium Sorta, edited by N. Degiuli, K. Žiha, N. Flesch, S. Šoda-Cotić, and V. Kokeza (2016), pp. 127–133.
[68]Y. Choi, B. Benjamin, S. Seng, G. Ducrozet, L. Gentaz, and P. Ferrant, "Generation of regular and irregular waves in Navier–Stokes CFD solvers by matching with the nonlinear potential wave solution at the boundaries," in *Proceedings of the ASME 2018 37th International Conference on Ocean, Offshore and Arctic Engineering* (ASME, NY, 2018), Paper No. V002T08A020.
[69]B. Quinn, "Validation of the high order spectral (HOS) method for extreme and breaking waves and coupling of the HOS-numerical wave tank model with OpenFOAM," M.S. thesis (University of Stavanger, Stavanger, Norway, 2019).
[70]Y. Zhuang, W. Zhao, and D. Wan, "The nonlinearity of scattering waves due to interaction between focusing waves and floating production storage and offloading," Phys. Fluids **35**(10), 107113 (2023).
[71]K. Shi and R. Zhu, "Efficient spectral coupled boundary element method for fully nonlinear wave–structure interaction simulation," Phys. Fluids **35**(5), 057121 (2023).
[72]C. M. Xie, J. C. Yang, P. N. Sun *et al.*, "An accurate and efficient HOS-meshfree CFD coupling method for simulating strong nonlinear wave–body interactions," Ocean Eng. **287**, 115889 (2023).
[73]C. Xie, J. Yang, P. Sun *et al.*, "An efficient HOS-SPH-BEM coupling method for wave-structure interaction problems," in *International Conference on Offshore Mechanics and Arctic Engineering* (American Society of Mechanical Engineers, 2024), Vol. 87820, Paper No. V05AT06A015.